X-ray Spectroscopic Study of the Electronic Structure of a Trigonal High-Spin Fe(IV)═O Complex Modeling Non-Heme Enzyme Intermediates and Their Reactivity

DOI:
10.1021/jacs.3c06181

Document Version
Accepted author manuscript

Published in:
Journal of the American Chemical Society

X-ray spectroscopic study of the electronic structure of a trigonal high spin Fe(IV)=O complex modeling non-heme enzyme intermediates and their reactivity

Augustin Braun,[†,‡] Leland B. Gee,[†,‡] Michael W. Mara,[†,‡,¶] Ethan A. Hill,[§,‖] Thomas Kroll,[‡] Dennis Nordlund,[‡] Dimosthenis Sokaras,[‡] Pieter Glatzel,[⊥] Britt Hedman,[*,‡] Keith O. Hodgson,[*,†,‡] A. S. Borovik,[*,§] Michael L. Baker,[*,#,@,†,‡] and Edward I. Solomon[*,†,‡]

†*Department of Chemistry, Stanford University, Stanford, California 94305, United States*

‡*Stanford Synchrotron Radiation Lightsource, SLAC National Accelerator Laboratory, Stanford University, Menlo Park, California 94025, United States*

¶*Present address: Department of Chemistry, Northwestern University, Evanston, Illinois 60208, United States; Chemical Sciences and Engineering Division, Argonne National Laboratory, Lemont, Illinois 60439, United States*

§*Department of Chemistry, University of California, Irvine, California 92697, United States*

‖*Present address: Department of Chemistry and Biochemistry, Auburn University, Auburn, Alabama 36849, United States*

⊥*ESRF The European Synchrotron, 71 Avenue des Martyrs, 38000 Grenoble, France*

#*Department of Chemistry, The University of Manchester, Manchester M13 9PL, United Kingdom*

@*The University of Manchester at Harwell, Diamond Light Source, Harwell Campus, OX11 0DE, UK*

E-mail: bhedman@stanford.edu; hodgsonk@stanford.edu; aborovik@uci.edu; michael.baker@manchester.ac.uk; edward.solomon@stanford.edu

Abstract

Fe K-edge X-ray absorption spectroscopy (XAS) has long been used for the study of high-valent iron intermediates in biological and artificial catalysts. 4p-mixing into the 3d orbitals complicates the pre-edge analysis but when correctly understood via 1s2p resonant inelastic X-ray scattering (RIXS) and Fe L-edge XAS, enables deeper insight into geometric structure and correlates with the electronic structure and reactivity. This study shows that in addition to the 4p-mixing into 3d(z^2) orbital due to the short iron-oxo bond, the loss of inversion in the equatorial plane leads to 4p mixing into the 3d(x^2-y^2,xy), providing structural insight and allowing the distinction of 6- vs. 5-coordinate active sites as shown through application to the Fe(IV)=O intermediate of taurine dioxygenase. Combined with O K-edge XAS, this study gives an unprecedented experimental insight into the electronic structure of Fe(IV)=O active sites and their selectivity for reactivity enabled by the π-pathway involving the 3d(xz/yz) orbitals. Finally, the large effect of spin polarization is experimentally assigned in the pre-edge (i.e. the α/β splitting) and found to be better modeled by multiplet simulations rather than by commonly used time-dependent density functional theory.

1. Introduction

Mononuclear non-heme iron enzymes activate O_2 to catalyze a wide range of chemical reactions in nature, ranging from natural product biosynthesis to bioremediation and DNA repair.[1–4] A subgroup of enzymes use α-ketoglutarate (αKG) or pterin as a cofactor to provide two electrons for the activation of O_2. They employ a two-histidine/one-carboxylate facial triad binding a high spin Fe(II) to activate O_2 in the presence of both bound cofactor and substrate to form high spin S=2 Fe(IV)=O intermediates.[5] In the αKG-dependent enzymes, these perform H atom abstraction on their substrate for hydroxylation, halogenation, desaturation, epimerization, ring closure and ring rearrangements.[6]

Taurine dioxygenase (TauD), which was the first αKG-dependent enzyme whose O_2-

intermediate was generated,[7] and the syringomycin halogenase SyrB2,[8] which has a chloride or bromide in place of the carboxylate residue, have been studied over the last two decades to investigate the geometric and electronic structure and reactivity of these Fe(IV)=O intermediates through kinetics, Mössbauer spectroscopy, X-ray absorption spectroscopy (XAS), resonance Raman, magnetic circular dichroism (MCD), nuclear resonance vibrational spectroscopy (NRVS) and calculations.[9–17] In particular, NRVS was used to determine for SyrB2[14] and TauD[15] that the Fe(IV)=O intermediate had a five-coordinate distorted trigonal bipyramidal geometries (Figure 1A). These intermediates inspired the synthesis of model complexes.[18] While most attempts to synthesize Fe(IV)=O molecules yielded six-coordinate S=1 model complexes,[19,20] the introduction of bulky tripod ligands enforcing a five-coordinate geometry allowed the synthesis of S=2 Fe(IV)=O centers,[21,22] in particular for this study $[Fe(IV)O(H_3buea)]^-$ ($[H_3buea]^{3-}$ = tris[N'-tert-butylureaylato-N-ethylene]aminato) (Figure 1B), due to the trigonal ligand field splitting of the 3d orbitals (Figure 1C).

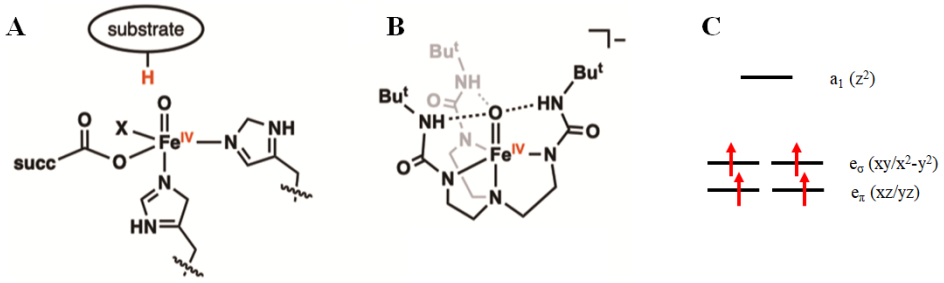

Figure 1: A) NRVS-determined trigonal bipyramid structure[14,15] of the Fe(IV)=O intermediate of TauD (X=Asp) / SyrB2 (X=Cl or Br). B) Structure of the five-coordinate $[Fe(IV)O(H_3buea)]^-$ complex.[22] C) Schematic molecular orbital diagram of a trigonal high spin Fe(IV)=O complex.

In the past literature, Fe K-edge XAS has contributed to the study of Fe(IV)=O intermediates[23–27] as these have characteristically intense pre-edges that arise from the loss of inversion in the axial direction, leading to a strong mixing of the Fe $4p_z$ orbital into the $3d(z^2)$, resulting in intense electric dipole-allowed character in the $1s \rightarrow 3d(z^2)$ transition.[28] However, additional information can be extracted from the Fe K-pre-edge by measuring 1s2p resonant inelastic X-ray scattering (1s2p RIXS) in combination with Fe L-edge XAS.[29–31] Di-

agonal cuts through the RIXS plane at constant emission energy give Fe K-edge-like spectra with higher energy resolution than the standard K-edge XAS experiment due to the long-lived 2p core-hole final state, enabling the resolution of distinct spectral features. Vertical cuts at constant incident energy through these features of the K-pre-edge enable their correlation with the Fe L-edge XAS, allowing specific spectral assignments. In our previous study of ferric-oxo dimer species,[32] this approach showed that while allowed by group theory in C_{4v} symmetry, the Fe $4p_{x,y}$ orbitals do not mix significantly into the 3d(xz,yz) orbitals, in contrast to the intense $4p_z$ mixing into the $3d(z^2)$ orbital. In the present study, we use a parallel approach on the five-coordinate trigonal bipyramidal (C_{3v} symmetry) S=2 Fe(IV)=O site in the model complex $[Fe(IV)O(H_3buea)]^{-}$ [22] (Figure 1B), calibrated by the two parent high spin ferric oxo and hydroxo complexes $[Fe(III)O(H_3buea)]^{2-}$ [33] and $[Fe(III)(OH)(H_3buea)]^{-}$ [34] to determine that the additional structure we observe in the K-pre-edge is due to the non-centrosymmetric equatorial trigonal ligand field that results in mixing of the $3d(xy,x^2\text{-}y^2)$ with the $4p_{x,y}$ orbitals and to the large exchange splitting of the α and β z^2 transitions. Having gained this insight from the model complexes, the methodology is extended to the structural determination of the Fe(IV)=O intermediate of TauD from the Fe K-edge XAS spectrum.

In addition, we use O K-edge XAS to experimentally quantify the oxo character in the frontier molecular orbitals that are key to the electrophilic and H atom abstraction reactivity of S=2 Fe(IV)=O active sites. While Fe L-edge XAS involves Fe 2p $\rightarrow$ 3d transitions and probes the 3d character in the valence metal orbitals[35–37] (i.e. the differential orbital covalency, DOC), O K-edge XAS involves transitions into the Fe 3d orbitals with O character and provides a direct probe of the covalencies of the Fe(IV)=O bonds as the intensity quantifies the oxo-character mixed into the different Fe 3d orbitals.[38,39] A range of computational studies has considered the difference in σ vs. π-reactivity of Fe(IV)=O species with different substrates,[13–15,17,40] where the σ-pathway enables an axial approach of the substrate along the Fe-O bond while the π-pathway enables an equatorial approach perpendicular to the

Fe-O bond. Our O K-edge XAS data and analysis provides unprecedented confirmation of the importance of the π-pathway through its more covalent π-bond.

2. Results and analysis

2.1. Fe K-edge XAS, RIXS and CEE

2.1.1. Experimental spectra

The 2D RIXS planes of the [Fe(III)(OH)(H_3buea)]$^-$, [Fe(III)O(H_3buea)]$^{2-}$ and [Fe(IV)O(H_3buea)]$^-$ complexes are shown on Figure 2. The incident photon, energy plotted on the x-axis, excites an Fe 1s electron into unoccupied 3d valence orbitals and results in 2p $\rightarrow$ 1s electronic relaxation with emission of a fluorescence photon. The y-axis is plotted as the energy transfer, that is the energy difference between the incident photon and the emitted photon. Cuts through the RIXS plane at a constant emission energy (CEE, diagonal cuts of the RIXS plane shown as black lines in Figure 2) give Fe K-edge-like spectra with higher energy resolution than the standard K-edge XAS experiment, and cuts at constant incident energy (CIE, vertical cuts of the RIXS plane shown as an magenta line in Figure 2A) give Fe L-edge-like spectra with enhanced intensity for the transitions that are accessible from the intermediate K-pre-edge states reached at the incident energy. These are analyzed in section 2.2.

The Fe K-pre-edge XAS and CEE cuts (Figure 2D-F) give the electric quadrupole 1s $\rightarrow$ 3d transitions, but with a few percent Fe 4p character mixed into some of the 3d orbitals in these non-centrosymmetric complexes.[28] This results in 1s $\rightarrow$ 4p electric dipole contributions to the pre-edge intensity, that is about a hundred times stronger than a pure quadrupole-allowed 1s $\rightarrow$ 3d transition.[41] As a consequence, even a limited amount of 4p mixing can dominate the spectral shape of the Fe K-pre-edge.

The pre-edge of [Fe(III)(OH)(H_3buea)]$^-$ (Figure 2D) has a single intense feature at 7113.5 eV that dominates the spectrum, with a total pre-edge intensity of 16.8 units. The pre-edge

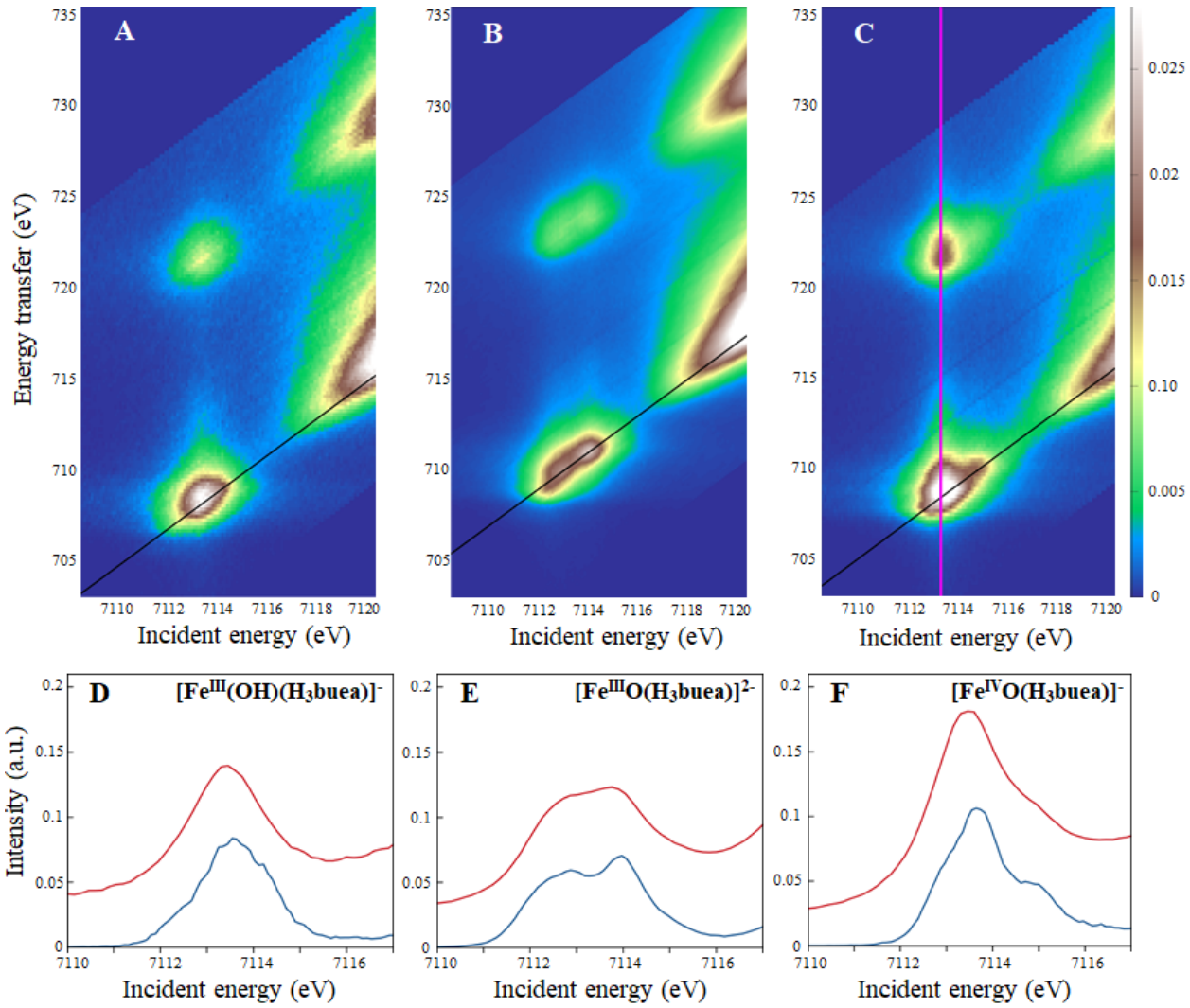

Figure 2: Experimental 1s2p RIXS planes of A) [Fe(III)(OH)(H_3buea)]$^-$, B) [Fe(III)O(H_3buea)]$^{2-}$ and C) [Fe(IV)O(H_3buea)]$^-$. The planes are normalized to the edge jump and plotted such that the maximum of intensity is in the pre-edge region. Diagonal black lines show the CEE. A magenta vertical line shows a CIE. (D-F) Corresponding CEE cuts (blue) and Fe K-edge XAS spectra (red).

of [Fe(III)O(H_3buea)]$^{2-}$ (Figure 2E) has a spectral shape with two intense features at 7112.9 and 7113.9 eV, with a tail to lower energy. It has a pre-edge intensity of 23.5 units. The pre-edge of [Fe(IV)O(H_3buea)]$^{-}$ (Figure 2F) is dominated by an intense peak at 7113.6 eV with a low-energy shoulder at 7112.9 eV and a more pronounced high-energy shoulder at 7114.7 eV. These are better resolved in the CEE cuts of the RIXS planes (blue spectra in Figure 2D-F) than in the standard K-edge XAS spectra (red spectra). The pre-edge intensity for the Fe(IV)=O complex is significantly higher than for the ferric compounds with 38.2 units. Such high-intensity features in the pre-edges of all three compounds highlight the dominance of electric dipole intensity, even in the [Fe(III)(OH)(H_3buea)]$^{-}$ compound that does not have a significant axial Fe-O distortion.

For an S = 5/2 high spin molecule in an O_h environment, 1s to 3d transitions result in $^5T_{2g}$ and ^5E_g final states split in energy by 10 Dq[28] (a d^6 final state formalism is adopted here since the 1s core hole has a_{1g} symmetry and interacts negligibly with the valence electrons, *vide infra*). Both final states have purely electric quadrupole character with a low total pre-edge intensity around 6 units.[26,28] In the case of a trigonal bipyramidal high spin ferric D_{3h} complex (Figure 1C), three final states can be reached: ^{5}E' (xy, x^2-y^2), ^{5}E" (xz, yz) and ^{5}A'$_1$ (z^2). However, in D_{3h} symmetry, the local inversion symmetry is lost in the equatorial plane and the Fe $4p_x$ and $4p_y$ orbitals have E' symmetry and are allowed to mix with the 3d(xy) and 3d(x^2-y^2) orbitals, denoted e_σ. As shown previously,[42] 4p mixing into the 3d orbitals requires overlap of both of these metal 3d and 4p orbitals with the same ligand valence orbital. For D_{3h} symmetry, this interaction is in the equatorial (x,y) plane as shown in Figure 3 (A and B) and can lead to significant 3d/4p mixing. Therefore, the transitions into the 3d(e_σ) set can have significant electric dipole intensity. The 3d(xz) and 3d(yz) orbitals, denoted e_π, have e" symmetry in D_{3h} geometry and the 3d(z^2) orbital has a_1 symmetry and thus do not mix with the Fe 4p orbitals that have e' ($p_{x,y}$) and a"$_2$ (p_z) symmetry and the corresponding 1s $\rightarrow$ 3d transitions only have electric quadrupole intensity. Thus [Fe(III)(OH)(H_3buea)]$^{-}$, which has an effective D_{3h} symmetry as the transaxial ligands have similarly weak bonding

interactions with the iron center, exhibits a single intense feature in its pre-edge (the 1s to e_σ transition) with an intensity of 16.8 units (Figure 2D), about 10 units higher than the total pre-edge intensity of centrosymmetric high spin ferric compounds.[28] The peak at 7113.5 eV is thus assigned as the 1s $\rightarrow$ e_σ transition with mostly dipole character (induced by the equatorial trigonal ligand field). Its high intensity precludes the observation of the quadrupole transitions into the 3d e_π and z^2 orbitals.

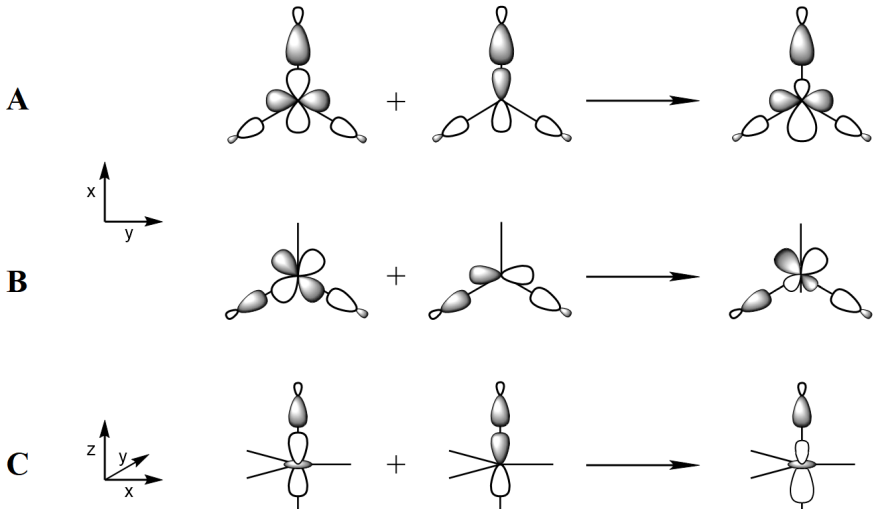

Figure 3: Schematics showing the 3d/4p mixing mechanism and the resultant metal-ligand 3d antibonding molecular orbital (on the right) for A) the metal $4p_x$ with the $3d(x^2\text{-}y^2)$, B) $4p_y$ with the 3d(xy) and C) $4p_z$ with the $3d(z^2)$ orbitals through the overlaps with the appropriate symmetry adapted linear combinations of ligand orbitals.

In going to $[Fe(III)O(H_3buea)]^{2-}$, the axial Fe-O bond is shorter than its transaxial counterpart (1.81 Å vs. 2.28 Å) and the molecule now has effective C_{3v} symmetry. The inversion symmetry is now also lost in the axial direction and the $3d(z^2)$ and $4p_z$ orbitals now both have a_1 symmetry. Since both orbitals have significant σ-overlap with the oxo ligand $2p_z$ donor orbital (Figure 3C), they mix and the corresponding 1s $\rightarrow$ $3d(z^2)$ transition gains electric dipole intensity. The e_σ orbitals have e symmetry in C_{3v} and still mix with the Fe $4p_{x,y}$. However, the e_π orbitals now also have e symmetry and can also mix with the $4p_{x,y}$ orbitals. As previously investigated in the oxo-bridged tetragonal compounds Fe_2-oxo-$(HBpz_3)_2(\mu\text{-}ac)_2$ and Fe_2-oxo-$hedta_2$,[32] while allowed by group theory in C_{4v} effective symmetry, the oxo-induced $4p_{x,y}$ mixing into the dπ-orbitals is small due to their poor π-overlap with the

oxo $2p_x$ and $2p_y$ orbitals. This is also the case for $[Fe(III)O(H_3buea)]^{2-}$. For this complex, the pre-edge intensity now increases to 23.5 units with two main features contributing to the spectral shape (Figure 2E). These correspond to the two dipole-allowed 1s $\rightarrow$ 3d e_σ and z^2 transitions, with the 1s $\rightarrow$ 3d e_π transition remaining a weak, mostly quadrupole transition, contributing much less to the pre-edge.

Finally, in going to the S=2 $[Fe(IV)O(H_3buea)]^-$ compound which also has C_{3v} symmetry, the z^2 α orbital is now also unoccupied. The 1s $\rightarrow$ z^2 α transition occurs at a lower energy than the 1s $\rightarrow$ z^2 β transition, because its exchange interaction with the four other α 3d electrons stabilize this excited state. The Fe-O bond is also shorter than in $[Fe(III)O(H_3buea)]^{2-}$ (1.68 Å vs. 1.81 Å), therefore the amount of 4p character mixed into the z^2 α and β orbitals and the total dipole intensity is higher. Thus, there are now formally two z^2 α and β transitions split by the energy difference of their exchange interactions. The equatorial trigonal ligand field still leads to $4p_{x,y}$ mixing in the $3d(e_\sigma)$ orbitals. The total pre-edge intensity increases to 38.2 and the pre-edge shape (Figure 2F) consists of three intense features at 7112.9, 7113.6 and 7114.7 eV, corresponding to the dipole-allowed transitions into the 3d e_σ, z^2 α and β orbitals. Specific assignments of the three peaks in (Figure 2F) are evaluated below.

2.1.2. DFT calculations

DFT calculations were performed to describe the ground state of the three model complexes. The results of the calculations are given in Figure 4 for $[Fe(IV)O(H_3buea)]^-$ and Figure S2 of the Supporting Material for $[Fe(III)O(H_3buea)]^{2-}$ and $[Fe(III)(OH)(H_3buea)]^-$. Note that the fully unoccupied β-manifold reasonably reflects the ligand field splitting of the Fe 3d orbitals without significant differences in spin polarization, while the partial occupation of the α-manifold results in its spin polarization.

From the energy diagram of the trigonal bipyramidal $[Fe(IV)O(H_3buea)]^-$ complex in Figure 4A, there is a small energy gap of 0.68 eV between the e_π and e_σ orbitals, and a

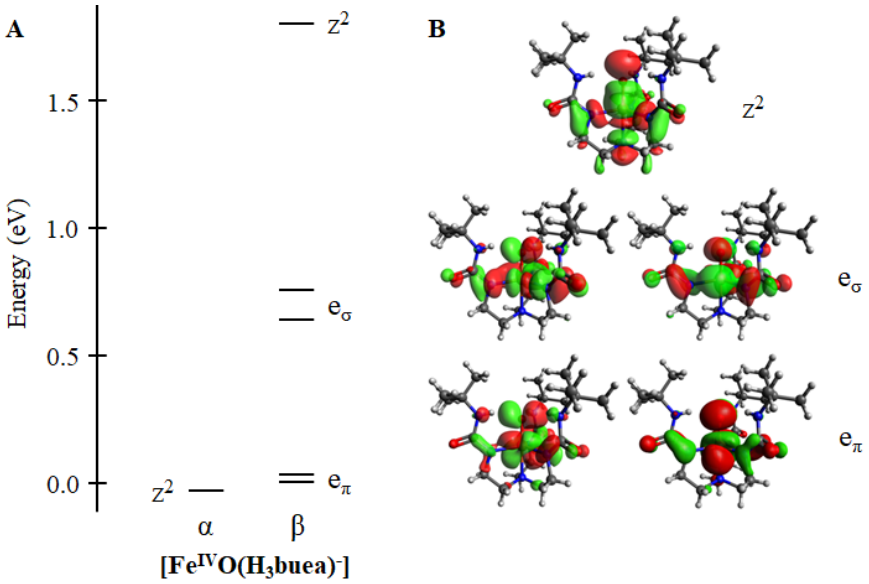

MO	d character
e_π β	67%
e_σ β	65%
z^2 α	43%
z^2 β	57%

Figure 4: A) Energy diagram of the unoccupied valence orbitals of $[Fe(IV)O(H_3buea)]^-$. The energy axis is shifted to set the lowest e_π β orbital to zero. B) Isosurface plots of the five 3d orbitals in the β-manifold of $[Fe(IV)O(H_3buea)]^-$. C) Löwdin population analysis of the unoccupied 3d orbitals of $[Fe(IV)O(H_3buea)]^-$. The C_{3v} averaged amount of Fe d-character is given for each orbital set.

larger gap of 1.11 eV between the e_σ and the z^2 in the β-manifold. Note that the two sets of e-orbitals mix and thus are tilted as described in more detail in Figure S3. We use here the e_π and e_σ notation for the orbital set with the most e_π and e_σ character, respectively. From the isosurface plots, the e_π orbitals (Figure 4B, bottom) are mostly localized on the iron and oxygen atoms and form the axial π-bond. The e_σ orbitals (Figure 4B, middle) reflect the interactions of the iron atom with the equatorial ligands, but the angles between the nitrogen atoms being close to 120° limits the σ-overlap of the 3d(e_σ) orbitals with all three atoms. The equatorial ligand field is therefore relatively weak resulting in the small energy gap between e_π and e_σ levels, and thus the high spin S=2 ground state. The similar energies of the e sets is also reflected in their similar calculated covalencies (65% vs. 67% Fe 3d character, Figure 4C). Finally, the 3d(z^2) β orbital (Figure 4B, top) is strongly σ-interacting mostly with the axial ligands, with 57% Fe 3d character (Figure 4C). For the Fe(IV)=O, the z^2 α orbital is the LUMO because of the strong spin polarization (Figure 4A). It has increased covalent mixing with the ligands and thus less Fe 3d character (43%).

Correlating from [Fe(IV)O(H_3buea)]$^-$ to [Fe(III)O(H_3buea)]$^{2-}$ and [Fe(III)(OH)(H_3buea)]$^-$, the energies of the e_σ and z^2 orbitals decrease relative to the e_π and the d-character of each orbital set increases (Figure S2), consistent with the ferric compounds being less covalent, with the Fe-O π- and σ-bonds becoming significantly weaker. These changes reflect the bond length changes in their crystal structures, where the average equatorial bond lengths increase from 1.98 Å to 2.06 Å and 2.02 Å, and the axial Fe-O bond length from 1.68 Å to 1.81 Å and 1.93 Å across the series: Fe(IV)=O to Fe(III)-O to Fe(III)-OH.[22,33,34]

2.1.3. Time-Dependent Density Functional Theory (TDDFT)

The Fe K-pre-edge XAS for the three compounds were calculated using TDDFT[26,43] and the simulated spectra are plotted in Figure 5, along with the corresponding experimental CEE spectra. The vertical stick heights in Figure 5 correspond to the intensities of the transitions (quadrupole plus dipole). The TDDFT-calculated total intensity (scaled to the experimental intensity) increases from 21.4 to 26.2 to 38.2 units through the series, consistent with the experimental trend (16.8 to 23.5 to 38.2). The spectral shapes are reasonably well reproduced and analyzed below, along with the assignments for the TDDFT-simulated spectra.

The TDDFT-simulated spectrum of [Fe(III)(OH)(H_3buea)]$^-$ (Figure 5A) has an intense peak as also observed in the experimental pre-edge data in Figure 5A, corresponding to the 1s transitions into the 3d(e_σ) orbitals, consistent with the non-centrosymmetric trigonal equatorial ligand field (Figure 3A and B). The transitions into the e_π and z^2 orbitals have mostly quadrupole character and thus are weak and produce the low and high energy tails, respectively, of the pre-edge spectrum.

The simulated spectrum of [Fe(III)O(H_3buea)]$^{2-}$ (Figure 5B) has two intense features similar to the experimental spectrum. The 1s $\rightarrow$ 3d(z^2) transition is at high energy and has high dipole intensity (shown as blue sticks). Two strong dipole-allowed transitions into a first set of e orbitals are calculated at 1.9 eV lower energy at 7111.9 eV (in green) with the transitions into the second set of e-orbitals having low intensity at 0.8 eV higher energy

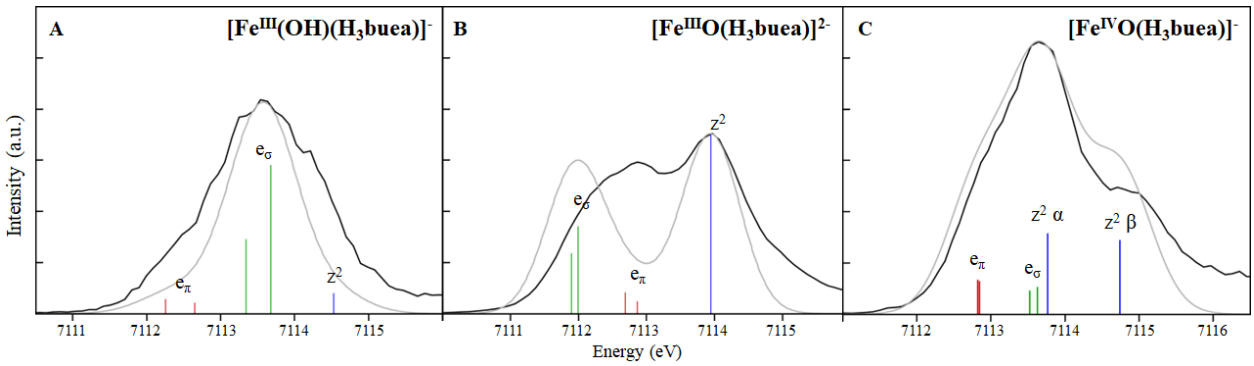

D

	Exp. intensity	TD-DFT intensity
$[Fe^{IV}O(H_3buea)]^-$	38.2	38.2 (reference)
$[Fe^{III}O(H_3buea)]^{2-}$	23.5	26.2
$[Fe^{III}(OH)(H_3buea)]^-$	16.8	21.4

Figure 5: TDDFT simulated spectra (in grey) of A) [Fe(III)(OH)(H_3buea)]$^-$, B) [Fe(III)O(H_3buea)]$^{2-}$ and C) [Fe(IV)O(H_3buea)]$^-$, each plotted with the corresponding experimental CEE (in black). The transitions are indicated by colored vertical lines: e_π in red, e_σ in green and z^2 in blue. The intensity of the simulations was scaled to the experimental intensity and their energy was shifted. D) Comparison of the experimental and TDDFT simulated intensities of the model complexes. The intensity of [Fe(IV)O(H_3buea)]$^-$ is used as a reference to scale the calculated intensities.

at 7112.7 eV (in red). Correlating to the CEE, the high energy e transitions at 7112.9 eV experimentally have more dipole character. Thus the TDDFT calculation overestimates the electronic relaxation due to the core 1s hole. The effect of electronic relaxation on the e levels can be observed from the comparison of the ground state MOs with the Natural Transition Orbitals (NTOs[44] which provide a chemically-intuitive picture of the orbitals involved in the transitions) (Figure S4). This electronic relaxation shifts the dipole character into the lowest energy e peak, while experimentally there is more intensity in the higher e energy peak in Figure 5B.

In the simulated spectrum of [Fe(IV)O(H_3buea)]$^-$ (Figure 5C), significant dipole intensity is found for all transitions into the six unoccupied acceptor Fe 3d orbitals, one α and five β transitions (Figure 4A). The visualizations of the NTOs (plotted in Figure S5) show that the four first transitions are into the e_π and at 0.7 eV higher energy the e_σ orbitals and have similar dipole intensity, and the two higher energy transitions are into the z^2 α and β orbitals with the z^2 α overlapping the e_σ set. As mentioned earlier, in the ground state, the two e

orbital sets are slightly tilted. In the NTOs (Figure S6) these are even more tilted, indicating further electronic relaxation in the final state. This mixing distributes the dipole character over both e sets. The transitions into the z^2 α and β orbitals are calculated by TDDFT to be split by 0.97 eV, reflecting the magnitude of their exchange interactions with the unpaired electrons. This is also functional-dependent, with lower amounts of Hartree-Fock exchange resulting in larger energy splittings of the z^2 α and β transitions (Table S3).

Thus the transitions corresponding to the 1s $\rightarrow$ e_σ excitations have significant electric dipole character for all three complexes, which reflects the mixing of the $4p_x$ and $4p_y$ with the 3d(xy) and 3d(x^2-y^2) orbitals, due to the trigonal equatorial symmetry enforced by the tripodal ligand as described above (Figure 3A and B). In the case of [Fe(IV)O(H_3buea)]$^-$, this $4p_{x,y}$ dipole character is strongly mixed over the two e sets. Moreover, the 1s $\rightarrow$ z^2 transitions of [Fe(III)O(H_3buea)]$^{2-}$ and [Fe(IV)O(H_3buea)]$^-$ gain electric dipole intensity in C_{3v}, due to the shorter Fe-O axial bond lengths that mix Fe $4p_z$ character into the 3d(z^2) orbitals (Figure 3C). Thus, for [Fe(IV)O(H_3buea)]$^-$, the TDDFT simulation (Figure 5C) agrees reasonably well with the experimental spectral shape. It assigns the three features as transitions into the e_π at lowest energy, at higher energy a main peak consisting of transitions into the e_σ and z^2 α orbitals, and the transition into the z^2 β at the highest energy. However, a multiplet analysis of this spectrum is presented below that gives a different assignment of the three peaks in the Fe K-pre-edge of the [Fe(IV)O(H_3buea)]$^-$ complex.

2.1.4. Multiplet analysis of the Fe K-pre-edge of [Fe(IV)O(H_3buea)]$^-$

Multiplet calculations were performed for [Fe(IV)O(H_3buea)]$^-$ in C_{3v} symmetry using Quanty.[45,46] Using the β-orbital energy splittings from the ground state DFT simulations presented above (Figure 4A), the energies of the $3d^5$ states for a trigonal complex, corresponding to the final states of the 1s $\rightarrow$ 3d transitions, were calculated with a systematic increase of the Slater integrals to allow for increasing electron-electron repulsion (Figure 6). The states reachable by a one-electron 1s $\rightarrow$ 3d transition from the $e_\sigma{}^2e_\pi{}^2$ ground state for a trigonal S=2 Fe(IV)=O

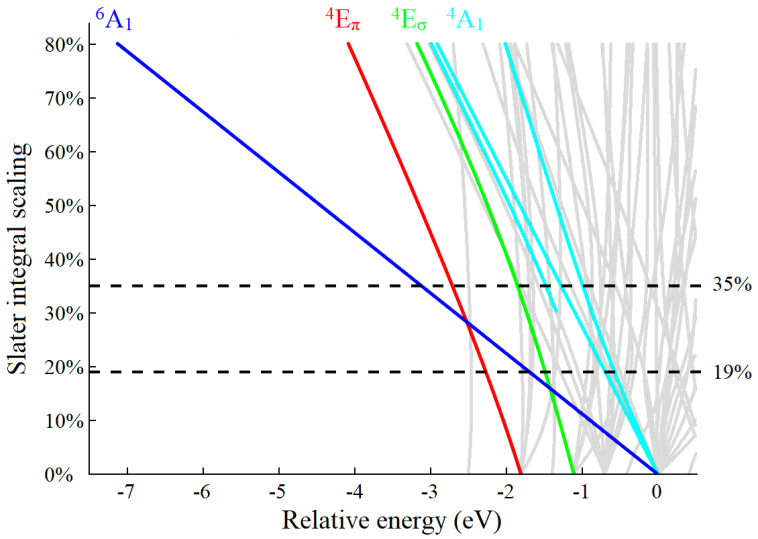

Figure 6: Energy diagram of the $3d^5$ final states of a trigonal S=2 Fe(IV)=O complex calculated as a function of the scaling of Hartree Fock Slater integrals from 0 (no electron repulsion) to 80%, using the DFT-calculated β-orbital energy splittings as input parameters. The E_π states reachable by a 1s $\rightarrow$ 3d transition are highlighted in red, E_σ in green and A_1 in blue. The grey lines are additional states that can only be reached by two-electron transitions from the ground state of the $e_\pi^2 e_\sigma^2$ configuration. The horizontal black lines indicate the scaling of the Slater integrals required to obtain a 1.8 and 1.1 eV splitting of the A_1 states.

complex are highlighted in red for E_π, green for E_σ and blue for A_1 states. Additional excited configurations ($e_\pi^4 e_\sigma^1$, $e_\pi^1 e_\sigma^4$, $e_\pi^4 a_1^1$, $e_\pi^3 e_\sigma^1 a_1^1$ and $e_\pi^1 e_\sigma^3 a_1^1$ in increasing energy order), shown in thiner grey lines, would be reached by two-electron excitations from the ground state and have negligible intensity in the Fe K-pre-edge. With no electron-electron repulsion (0% in Figure 6), the energy splittings between the three states in red, green and blue correspond to the β-orbital energy diagram in Figure 4A. When the electron-electron repulsion is included, the configurations increasingly split into many-electron final states. The increase in the Slater integrals corresponds to a decrease in the nephelauxetic reduction of electron repulsion (i.e. less covalency). Most notably, the $e_\pi^2 e_\sigma^2 a_1^1$ configuration splits into the $^6A_1$ and $^4A_1$ states. While the theoretical intensity ratio between the sextet and quartet states is 1.5 due to their difference in spin multiplicity, this ratio decreases with increasing multiplet interactions with other states. Multiplet interactions also further split the $^4A_1$ state. The $^4A_1$ are the highest energy states at all scaling values of the Slater integrals.

The experimental CEE for [Fe(IV)O(H_3buea)]$^-$ (Figure 2F) shows three peaks at 7112.9, 7113.6 and 7114.7 eV. The highest energy peak corresponds to these $^4A_1$ states (transition into the z^2 β). The splitting of the sextet and quartet A_1 states can therefore be either 1.1 or 1.8 eV depending on whether the $^6A_1$ states correspond to the 7113.6 or 7112.9 eV feature in the experimental CEE spectrum in Figure 2F. From Figure 6, the first assignment corresponds to a Slater integral scaled down to approximately 19% of its free ion value, and gives a similar assignment to the TDDFT calculations. Alternatively the assignment of the $^6A_1$ states as the lowest energy peak of the pre-edge corresponds to a Slater integral scaling of about 35%. In our previous study of the S=2 square pyramidal Fe(IV)=O α-O site in zeolites, we observed two intense peaks split by 1.6 eV,[47] that we can now assign as the transitions into the z^2 α and β orbitals of the tetragonal S=2 site. This splitting is close to the 1.8 eV splitting obtained for a 35% Slater integral scaling. The decrease in Slater integral scaling down to 35% is also consistent with the nephelauxetic decrease in electron-electron repulsion observed upon oxidation from Mn(II) to Mn(III) to Mn(IV). 19% is unreasonably low: multiplet simulations with such a low Slater integral scaling result in a low spin ground state ($e_\pi{}^4e_\sigma{}^0$ configuration) instead of the high spin ground state observed experimentally (more detailed comments on the Slater integral scaling are presented in the Supporting Information). Thus we can assign the peak at 7112.9 eV as the transition into the z^2 α orbital and the peak at 7114.7 eV as the transition into the z^2 β orbital.

The low- and high-energy peaks, at 7112.9 and 7114.7 eV respectively, corresponding qualitatively mostly to the A_1 states, were subtracted from the experimental CEE spectrum (Figure S7) to obtain an estimate of the remaining combined dipole contribution from the E_π and E_σ states. This subtraction produces an intense symmetric feature at 7113.6 eV, indicating that either the two sets of E states are at approximately the same energy or that the dipole intensity of the lower energy E_π states is negligibly low compared with the E_σ states. The multiplet simulations of the Fe L-edge XAS spectrum presented in section 2.2 below locks the energy position of the E_π at 0.95 eV below the E_σ states. This requires that

the intensity of the transitions into the e_π is not significant relative to the transitions into the e_σ, z^2 α and z^2 β, consistent with a low dipole character arising from the negligible $4p_{x,y}$ mixing into the e_π orbitals.

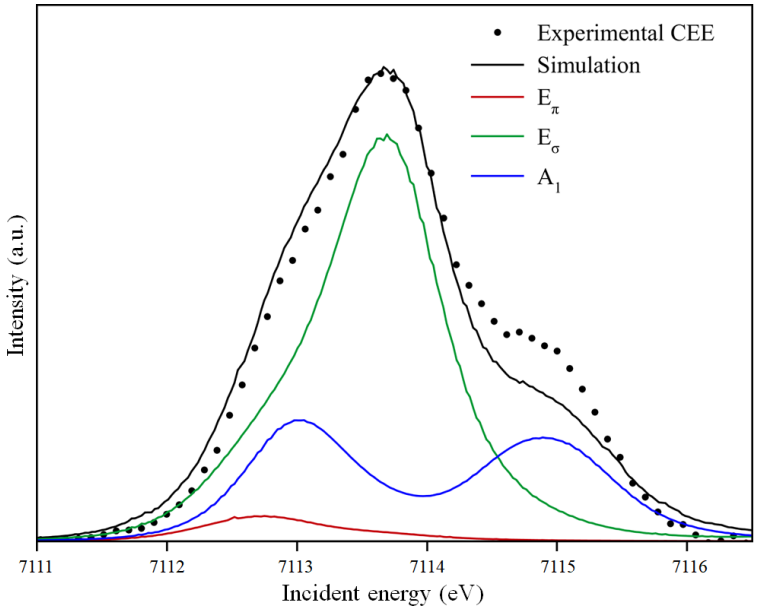

Figure 7: Multiplet-derived analysis of the CEE of $[Fe(IV)O(H_3buea)]^-$ using the atomic multiplet parameters in Table S1. Contributions from E_π states are in red, E_σ in green and A_1 in blue. See Supporting Information for details.

Using the above constraints, a good fit of the experimental CEE was obtained from the multiplet simulation and is plotted in Figure 7. Both the electric quadrupole (very small) and dipole contributions to the intensity are included in this simulation and the total intensity is scaled to the experimental spectrum. The main feature in the middle of the pre-edge (shown in green) corresponds mostly to $^4E_\sigma$ states. The low-energy shoulder has mostly $^6A_1$ contribution (blue), with weak $^4E_\pi$ (red) and $^4E_\sigma$ (green) contributions due to the mixing of those states. The high-energy feature has mostly $^4A_1$ contribution.

2.1.5. TDDFT vs. multiplet assignment of the Fe K-pre-edge XAS of $[Fe(IV)O(H_3buea)]^-$

As developed in the two previous sections, the TDDFT calculations and the multiplet simulations of the Fe K-pre-edge of $[Fe(IV)O(H_3buea)]^-$ lead to two different assignments of its three-peak CEE spectral shape in Figure 2F. The TDDFT simulation in Figure 5C indicates

a 1.1 eV-splitting of the $4p_z$-mixed 1s $\rightarrow$ z^2 α and β transitions, with one set of $4p_{x,y}$-mixed 1s $\rightarrow$ e transitions on the lower energy side of the z^2 α transition and the other set of 1s $\rightarrow$ e transitions overlapping the 1s $\rightarrow$ z^2 α transition. Alternatively, the multiplet simulation gives a 1.8 eV-splitting of the transitions into the z^2 α and β with the dipole-mixed 1s $\rightarrow$ e_σ transitions in between and the 1s $\rightarrow$ e_π transition at lower energy with little intensity (Figure 7). We explained in the previous section that the latter case with a Slater integral scaling around 35% is reasonable for Fe(IV) while 19% is not. These results indicate that the TDDFT calculations of the 1s $\rightarrow$ 3d transitions significantly underestimate the z^2 α/β exchange splitting.

The TDDFT simulation of the O K-edge XAS spectrum in section 2.3 below using the same B3LYP functional gives a splitting of the 1s(O) $\rightarrow$ z^2 α and β transitions of 1.89 eV vs. 0.97 eV for the Fe K-edge. This difference reflects the different interaction of the valence electrons with the 1s(O) core hole in the final state instead of a 1s(Fe) core hole for the Fe K-edge XAS calculations. As for the O K-edge XAS the z^2 α and β accepting orbitals are mostly localized on the Fe atom and the 1s(O) core hole is on the separate oxo atom, the exchange interactions of the valence electrons with the core are very small. Therefore, the smaller α/β splitting from the Fe K-edge XAS calculations indicates that the exchange interaction of the 1s(Fe) core hole with the valence 3d orbitals is overestimated by DFT, and this decreases the α/β splitting energy. For the Fe pre-edge (Figure 8A), the transition into the z^2 α orbital is destabilized by the interaction of the valence α-electrons with the core 1s(Fe) β-electron, while the transition into the z^2 β orbital is stabilized by interaction of the valence α-electrons with the core 1s(Fe) α-electron. This core/valence interaction opposes the valence/valence stabilization of the 3d(z^2) α state by exchange interaction with the α 3d electrons compared with the 3d(z^2) β state, and leads to the calculated decrease in the α/β splitting. For the O K-pre-edge (Figure 8B), the interaction of the valence electrons on the Fe atom with the 1s(O) core hole is negligible and the magnitude of the exchange splitting is not impacted.

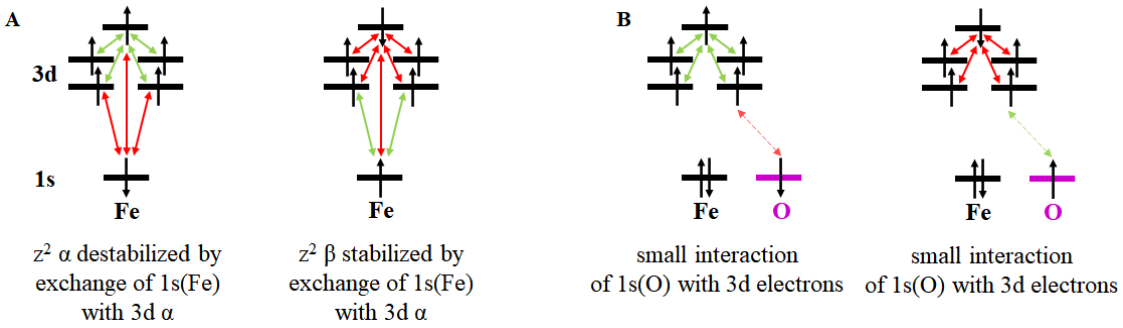

Figure 8: Schematics of the exchange interactions between electrons for 1s $\rightarrow$ 3d α and β transitions at the S=2 Fe(IV)=O center for A) Fe K-edge XAS and B) O K-edge XAS. The green arrows indicate stabilizing interactions while the red arrows indicate destabilizing interactions. The interactions with the 1s(O) core hole are negligibly small.

The core-valence exchange is governed by the Slater integral G_2(1s,3d). To evaluate the effect of G_2(1s,3d) on the splitting of the 1s $\rightarrow$ z^2 α and β transitions, multiplet simulations on the S=2 Fe(IV) complex were performed with all parameters fixed to the atomic multiplet value in Table S1 but with G_2(1s,3d) varied. As seen in Figure S8, a value around 1.0 eV for G_2(1s,3d) would be required to decrease the splitting of the $^6A_1$ and $^4A_1$ states to 1.1 eV as observed in TDDFT, much higher than the Hartree-Fock calculated value of 0.073 eV. Hard X-ray photoemission spectroscopic (HAXPES) data on Fe 1s ionization on iron oxides have been reported and no exchange splitting of the main line or the satellite peaks was observed,[48] indicating that the value of G_2(1s,3d) cannot be as high as 1 eV.

2.2. Fe L-edge XAS and CIEs of [Fe(IV)O(H_3buea)]$^-$

In an Fe L-edge XAS experiment, the incident photon excites an Fe 2p electron into unoccupied Fe 3d valence orbitals via electric dipole-allowed 2p $\rightarrow$ 3d transitions. While the Fe K-edge XAS spectrum of [Fe(IV)O(H_3buea)]$^-$ is dominated by the transitions into the 4p-mixed Fe 3d orbitals, Fe L-edge XAS is not sensitive to 4p mixing and thus directly probes the Fe 3d character of all valence final states. Specifically for the C_{3v}-symmetric [Fe(IV)O(H_3buea)]$^-$ compound of focus in this study, Fe L-edge XAS provides a direct probe of all 3d states, including those involving transitions into the e_π orbitals which have negligible

intensity in the Fe K-edge XAS spectrum.

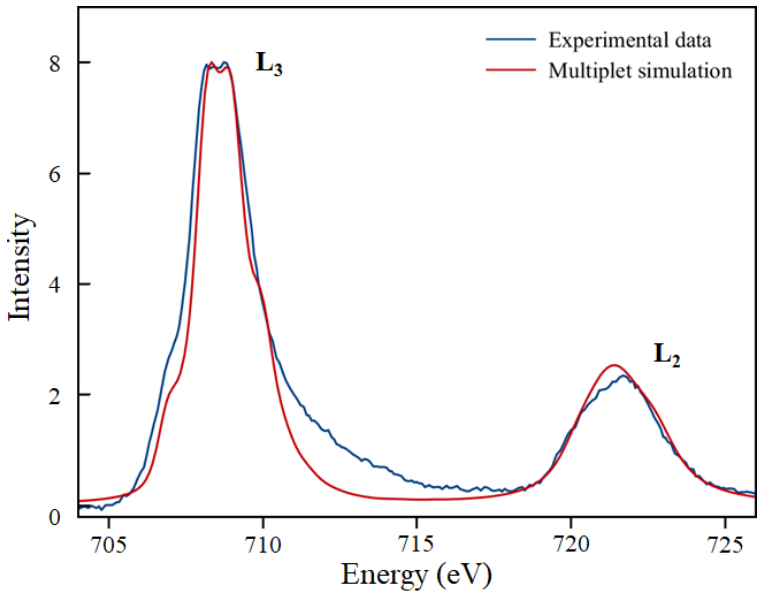

Figure 9: Background-subtracted Fe L-edge XAS spectrum of $[Fe(IV)O(H_3buea)]^-$ (blue) and multiplet simulation of the spectrum (red) using the atomic multiplet parameters in Table S1.

The background-subtracted Fe L-edge XAS spectrum of $[Fe(IV)O(H_3buea)]^-$ is shown in Figure 9 and the Fe L-edge XAS spectra of $[Fe(III)O(H_3buea)]^{2-}$ and $[Fe(III)(OH)(H_3buea)]^-$ are shown in the Supporting information (Figure S9). The Fe L-edge XAS spectrum of the $[Fe(IV)O(H_3buea)]^-$ complex shows several characteristic features. The main feature of the L_3-edge at 708.5 eV has a flat top with a low-energy shoulder at 707 eV and a high-energy tail.

Multiplet calculations were performed to simulate the Fe L-edge XAS of $[Fe(IV)O(H_3buea)]^-$. Most of the atomic and ligand field parameters including the scaling of the Slater integrals and the energies of the Fe 3d z^2 and e_σ orbitals were constrained by the Fe K-edge XAS spectrum (as presented in section 2.1.4). Only the energy of the e_π orbitals (Figure S10) and the linewidth were adjusted to obtain a good fit to the Fe L-edge XAS (Figure 9). Importantly, the multiplet simulations of the Fe L-edge XAS spectrum locks in the 3d e_π orbital energy at 0.68 eV below the e_σ orbital energy in order to reproduce the low-energy side of the L_3-edge (Figure S10). This splitting is consistent with the DFT-calculated ground state

energy diagram in Figure 4A and determined the energy positions of the 1s → e_π transitions that were used to assign the Fe K-edge XAS spectrum (Figure 7, red).

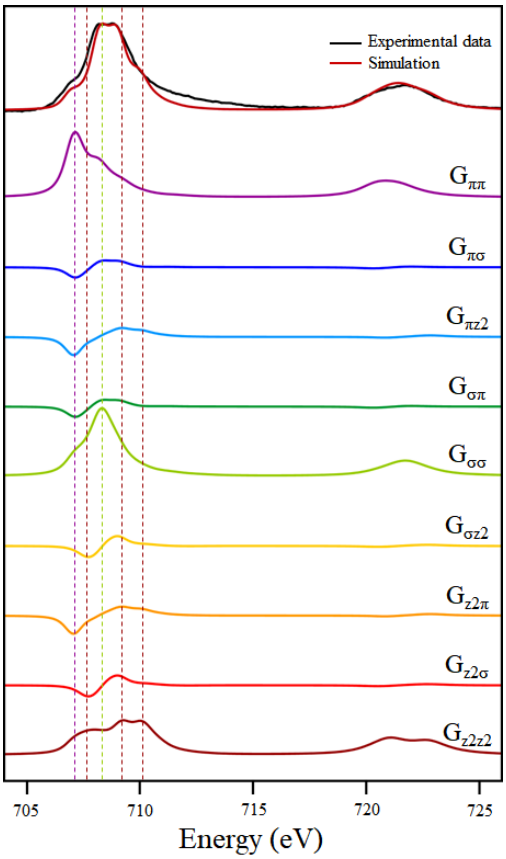

Figure 10: Correlation of the G_{ij} components of the calculated transition dipole tensor with the experimental Fe L-edge XAS spectrum (top). The σ subscript indicates the e_σ orbitals and the π subscript indicates the e_π orbitals. The vertical dashed lines indicate the maxima of the G_{ii} (purple for $G_{\pi\pi}$, light green for $G_{\sigma\sigma}$ and dark red for $G_{z^2z^2}$.

While the orbital contributions to the L-edge spectrum are distributed over a wide energy range due to 2p/3d spin-exchange, the components of the transition dipole operator matrix in the ligand field basis (G_{ij}, i, j=e_π, e_σ, z^2) indicate the contribution of each orbital to the Fe L-edge XAS spectrum (Figure 10). The diagonal terms G_{ii} indicate the dominant contributions while the off-diagonal terms G_{ij} ($i \neq j$) give the intensity redistribution due to the exchange. Consistent with Figure S10, the low-energy shoulder of the L_3-edge has mostly E_π-character governed by the $G_{\pi\pi}$ component (purple vertical dashed lines in Figure 10). The $G_{\sigma\sigma}$ (light green vertical dashes) contributes at higher energy in the main peak and the $G_{z^2z^2}$ (dark red

vertical dashes) is spread over the whole L_3-edge, consistent with the large exchange splitting of the sextet and quartet states. A multiplet simulation and G_{ij} decomposition of the Fe L-edge XAS spectrum including DOC[35–37] is shown in Figure S11; no significant change is observed in comparison with the atomic multiplet simulation presented here.

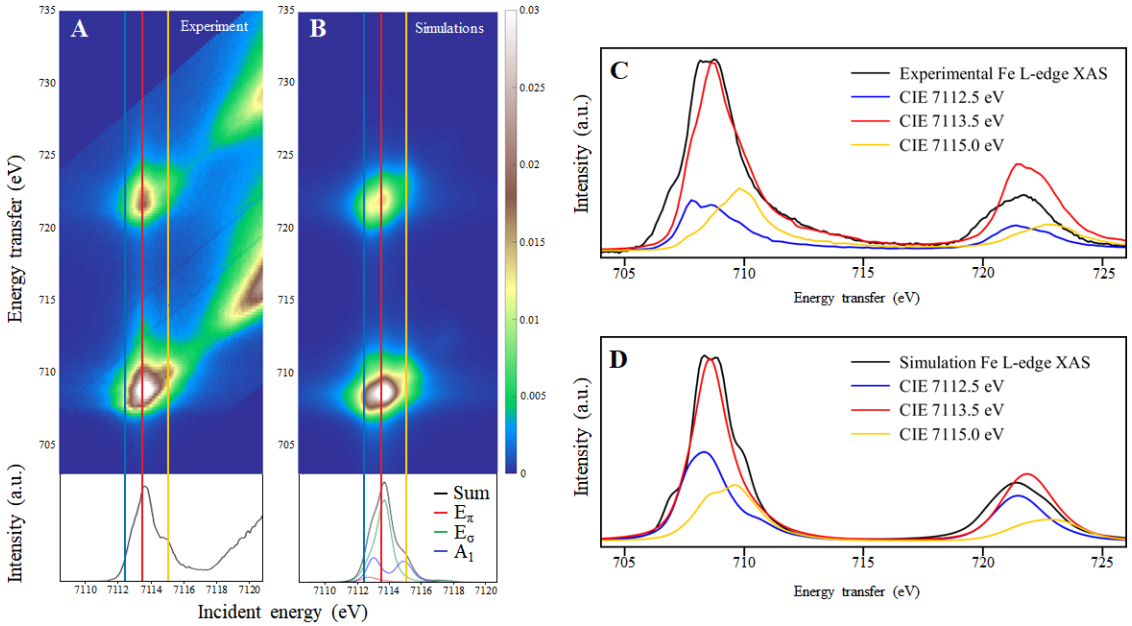

Figure 11: A) Experimental 1s2p RIXS plane of $[Fe(IV)O(H_3buea)]^-$ with the CEE shown in the bottom. The three vertical lines indicate the position of the three CIE cuts at 7112.5 eV (blue), 7113.5 eV (red) and 7115.0 eV (yellow). B) Corresponding multiplet-simulated RIXS plane and CIEs. C) Overlap of the experimental Fe L-edge XAS spectrum (black) with the CIE cuts from Figure 11A. D) Corresponding multiplet-simulated Fe L-edge XAS spectrum and CIE cuts Figure 11B.

This assignment of the Fe L-edge XAS spectrum enables further insight into the Fe K-edge XAS and 1s2p RIXS. CIE cuts of the RIXS plane are L-edge like spectra where the choice of the incident energy allows the enhancement of the corresponding L-edge final states, but while the Fe L-edge XAS spectrum reflects all the dipole-allowed 2p $\rightarrow$ 3d transitions, the CIEs are biased by the 4p-mixing into the 3d orbitals they probe. The CIE cuts in Figure 11C are at incident energies of 7112.5, 7113.5 and 7115.0 eV, corresponding mostly to the enhancement of $^6A_1$ (and $^4E_\sigma$ due to band overlap), $^4E_\sigma$ and $^4A_1$ final states, respectively, as determined in section 2.1.4. The $^4E_\pi$ states that make significant contributions to the Fe L-edge XAS spectrum ($G_{\pi\pi}$ in Figure 10) are not probed by 1s2p RIXS since they have

no significant 4p-mixing and therefore their contribution to the CIE cuts in Figure 11A and C is negligible. Indeed, none of the CIEs through the three intense features of the CEE at 7112.5, 7113.5 and 7115.0 eV show intensity in the low-energy shoulder at 706.8 eV where the $^4E_\pi$ states appear in the Fe L-edge XAS spectrum ($G_{\pi\pi}$ in Figure 10). This couples the assignments of both the Fe K-edge and L-edge XAS spectra. A detailed description of the CIEs and their simulations is found in Figure S12.

2.3. Oxygen K-edge XAS

While the Fe K-edge, L-edge XAS and 1s2p RIXS allow the quantification of the Fe 3d character in the valence orbitals, the reactivity of Fe(IV)=O sites is dictated by the oxo character in the dπ and dσ orbitals. In an O K-edge XAS experiment, the incident photon excites an O 1s electron into the unoccupied valence 3d orbitals. The 1s is localized on the oxygen atom and the 1s $\rightarrow$ 2p transition is electric dipole allowed, thus the transition intensity reflects the O 2p character in the 3d acceptor orbitals, i.e. their oxo covalencies. The [Fe(IV)O(H_3buea)]$^-$, [Fe(III)O(H_3buea)]$^{2-}$ and [Fe(III)(OH)(H_3buea)]$^-$ compounds have four O atoms (one is the axial oxo/hydroxide ligand and three are on the $[H_3buea]^{3-}$ ligand as shown in Figure 1B). Thus the O K-edge XAS spectra have contributions from transitions involving the 1s orbitals of all four O atoms. The spectra of [Fe(IV)O(H_3buea)]$^-$, [Fe(III)O(H_3buea)]$^{2-}$ and [Fe(III)(OH)(H_3buea)]$^-$ are shown on Figure 12A.

All three compounds have intense features at 532 eV with similar intensities. These features can be assigned as the transitions from the three ligand O 1s orbitals into the $\pi^*_{C=O}$ of the urea moieties of $[H_3buea]^{3-}$. The intensity variation of these features in Figure 12A is mostly due to the perturbation of the C=O bond of the urea moieties upon changes in the H-bond between the N-H part of the urea groups and the axial O ligand: the significantly more basic ferric oxo compound has a stronger H-bond, which polarizes the urea, increasing the coefficient of the nitrogen atom and decreasing the oxygen character in the $\pi^*_{C=O}$ relative to the two other compounds. At lower energies are the pre-edge transitions into the Fe 3d

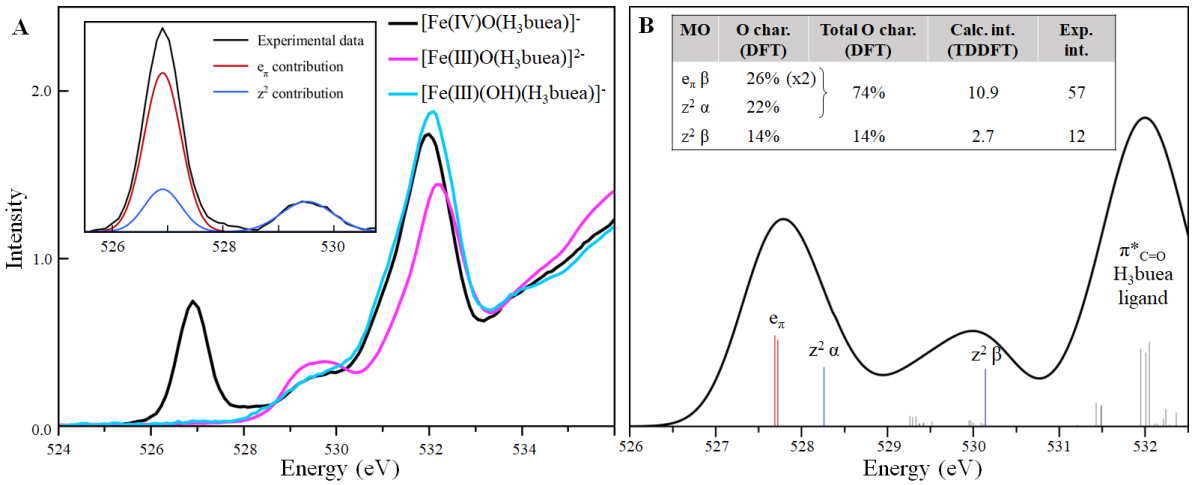

Figure 12: A) O K-edge XAS spectra of $[Fe(IV)O(H_3buea)]^-$ (black), $[Fe(III)O(H_3buea)]^{2-}$ (pink) and $[Fe(III)(OH)(H_3buea)]^-$ (blue). The inset shows the background subtracted pre-edge of $[Fe(IV)O(H_3buea)]^-$ (black) and its decomposition into the transitions into the e_π in red and into the z^2 α and β in blue (assuming transitions into the z^2 α and β have the same intensity). B) TDDFT simulated O K-edge XAS spectrum of $[Fe(IV)O(H_3buea)]^-$. The transitions indicated in grey involve ligand urea O atoms (used for energy calibration). The inset gives the comparison of the DFT-calculated O character of individual Fe 3d orbitals of $[Fe(IV)O(H_3buea)]^-$ in the ground state with the experimental intensity corresponding to the two observed features, and their TDDFT-calculated intensities.

orbitals, originating from the axial oxo/hydroxo ligand O 1s orbital, since only this oxygen atom has orbital overlap and thus covalent mixing with the Fe 3d orbitals. After background subtraction of the contribution of the transitions into the $\pi^*_{C=O}$ and higher energy transitions, the pre-edges of the three complexes are plotted in Figure S13. The pre-edges of the two ferric compounds start at approximatly the same energy, around 529.5 eV, with the pre-edge of $[Fe(III)(OH)(H_3buea)]^-$ (blue) being less intense than that of $[Fe(III)O(H_3buea)]^{2-}$ (pink). Importantly, the pre-edge of $[Fe(IV)O(H_3buea)]^-$ (black, inset in Figure 12) has a very intense low-energy feature at 527.0 eV and a weak feature at 529.5 eV.

Among the Fe 3d orbitals of the high spin ferric $[Fe(III)O(H_3buea)]^{2-}$ and $[Fe(III)(OH)(H_3buea)]^-$ compounds, the acceptor orbitals having O character from the axial ligand are the oxo 3d π-antibonding e_π orbitals and the oxo σ-antibonding 3d z^2 orbital of the β-manifold (Figure S2A). The e_σ orbitals only interact with the equatorial component of the $[H_3buea]^{3-}$ ligand and therefore have negligible axial O character. The lowest energy feature in the

spectra of [Fe(III)O(H_3buea)]$^{2-}$ and [Fe(III)(OH)(H_3buea)]$^{-}$ at 529.5 eV in Figure S2A then corresponds to transitions into their lowest energy 3d(e_π) orbitals. Based on Figure S2A, the transition into the z^2 orbital for both complexes should occur at about 1 eV higher in energy, and thus overlap the intense features of the ligand-based 1s $\rightarrow$ $\pi^*_{C=O}$ transitions at 532 eV.

Upon oxidation to the [Fe(IV)O(H_3buea)]$^{-}$ complex, the z^2 α orbital is now unoccupied and all β-transitions shift to lower energy as the effective nuclear charge Z_{eff} on the Fe atom has increased. From previous Cl K-pre-edge XAS measurements of model complexes, this shift to lower energy with one-electron oxidation is expected to be around 2 eV.[39] Thus, the O 1s transitions into the e_π β orbitals should contribute to the intense 527 eV feature in Figure 12A. From the MO energy diagram in Figure 4A, the energy gap between the e_π β and the z^2 β orbitals is around 2 eV. This leads to the assignment of the 529.5 eV feature to the O 1s transition into the 3d z^2 β orbital (Figure 12A). Due to the 2 eV-splitting of the z^2 α and β transitions (see above), the O 1s transition into the z^2 α orbital is expected to overlap the low-energy e_π feature at 527 eV. This assignment of the [Fe(IV)O(H_3buea)]$^{-}$ O K-edge XAS spectrum is consistent with the Löwdin population analysis of the ground state DFT calculations (Figure 12B, inset). The total calculated O character is 74% in the 527 eV feature (sum of e_π β and z^2 α O character) and 14% for the 529.5 eV feature (z^2 β O character), reasonably consistent with the intensity ratio of the 527 to 529.5 eV experimental features (5.3 for DFT-calculated vs. 4.8 for the experimental ratio). The z^2 α transition should have a similar covalency and thus intensity to that of the experimentally resolved z^2 β transition at 529.5 eV. The fact that the 527 eV feature has more than four times the intensity of the 529.5 eV feature indicates that the e_π β transitions make a major contribution to the intense feature at 527 eV of the experimental pre-edge. Using the intensity of the 529.5 eV z^2 β transition to estimate the z^2 α contribution to the 527 eV feature gives the π (red) and σ (blue) contributions shown in the inset of Figure 12A. This provides experimental evidence that each of the unoccupied e_π orbitals have high O character, about

twice that of the $3d(z^2)$ orbitals, giving a direct probe into this key contribution to the reactivity of Fe(IV)=O compounds (see Discussion). This is consistent with a previous electron paramagnetic resonance study on ^{17}O-labeled [Fe(IV)O(H_3buea)]$^-$ determining a significant spin density of 0.56 in the O p-orbitals which reflects the O character in the occupied e_π orbitals.[49] This enables the calibration of the intensity of the pre-edge in O K-edge XAS with 1.24% O character per unit of O K-pre-edge intensity.

The O K-pre-edge XAS spectrum of [Fe(IV)O(H_3buea)]$^-$ was simulated with TDDFT calculations using the B3LYP functional as shown in Figure 12B. Two O 1s $\rightarrow$ 3d features are calculated at 527.8 and 530.1 eV, lower in energy than calculated for the strong feature corresponding to the ligand-based O 1s $\rightarrow \pi^*_{C=O}$ transitions at 532 eV (used as a reference energy for the TDDFT calculations). Consistent with the above experimental assignment, the intense lowest energy feature at 527.8 eV consists of the overlapping transitions into the e_π β and z^2 α orbitals, while the high energy pre-edge feature at 530.1 eV corresponds to the transition into the z^2 β orbital. The intensity ratio of the two simulated features is 4.0 while the experimental value is 4.8. While the splitting of the 1s $\rightarrow$ z^2 α and β transitions was calculated to be 0.97 eV in the TDDFT-simulated Fe K-pre-edge, it is 1.88 eV in the TDDFT-simulated O K-pre-edge, much closer to the multiplet-calculated 1s-3d exchange splitting in section 2.1.4.

The O K-edge XAS, therefore, supports the Fe 1s $\rightarrow$ 3d K-pre-edge assignments based on the multiplet calculations, with the transitions into the e_π β and z^2 α orbitals close in energy but with the e_π orbitals having twice the oxo character of the z^2 orbitals, and with the z^2 α/β splitting close to 2 eV. The latter reflects the fact that in ligand K-edge XAS the 1s core hole is localized on the oxo ligand and thus has negligible exchange coupling with the 3d valence electrons that are mostly localized on the Fe center.

3. Discussion

While the 1s → 3d transitions observed in metal K-edge XAS are quadrupole allowed and give rise to only weak pre-edge absorption spectral features, the loss of inversion symmetry allows the mixing of some Fe 4p character into the 3d orbitals, leading to intense pre-edge transitions with 1s → 4p dipole character.[28] The distortion of an octahedron to an approximate C_{4v} geometry upon shortening one axial ligand bond is important in (bio)inorganic chemistry and a detailed study of this case was recently published.[32] This effective C_{4v} distortion gives rise to selective $4p_z$-mixing into the $3d(z^2)$ orbital leading to a strong 1s → $3d(z^2)/4p_z$ dipole-allowed transition. While the $4p_{x,y}$-mixing into the 3d(xz,yz) orbitals is allowed by group theory, the magnitude of this mixing is negligible because of the limited π-overlap of the $4p_{x,y}$ orbitals with the axial oxo ligand π-orbitals that enables this 3d/4p mixing.

The present study shows that other non-centrosymmetric distortions can also allow and result in significant 4p-mixing, as is the case for the trigonal iron centers studied here. Compared with the 1s → 3d spectrum of an octahedral high spin ferric compound, the spectrum of the approximate D_{3h} $[Fe(III)(OH)(H_3buea)]^-$ that does not have a short axial Fe-O bond still gains significant intensity through $4p_{x,y}$ mixing into the $3d(xy,x^2\text{-}y^2)$ orbitals as both sets of orbitals have significant σ-overlap with the equatorial tripod ligand (Figure 3A and B). The C_{3v}-symmetric $[Fe(III)O(H_3buea)]^{2-}$ and $[Fe(IV)O(H_3buea)]^-$ compounds thus have mixing of both the $4p_{x,y}$ with the $3d(xy,x^2\text{-}y^2)$ set and the $4p_z$ with the $3d(z^2)$ orbitals as the axial Fe(III)-O and Fe(IV)=O bonds are short and eliminate the inversion symmetry along the z-axis. As in the six-coordinate case, the $4p_{x,y}$ do not mix significantly with the 3d(xz,yz) orbitals as they have little π-overlap with the axial oxo ligand. Thus for both C_{3v} complexes, the $3d(z^2)$ and $3d(xy,x^2\text{-}y^2)$ have 4p-mixed character. However, the S=2 $[Fe(IV)O(H_3buea)]^-$ complex spectrum shows three pre-edge transitions due to the additional presence of the 1.8 eV splitting of the z^2 α and β orbitals that derives from their difference in exchange interactions with the 3d valence orbital electrons. The 1s transitions into the e_σ set energetically located in between the α/β z^2 transitions (Figure 7). This assignment

is derived from multiplet simulations and highlights an issue with TDDFT calculations, commonly used for the analysis of Fe K-edge XAS pre-edges,[26] to properly simulate the large exchange splitting of the z^2 α and β transitions in a high spin S=2 Fe(IV) system. Multiplet simulations fit the spectral shapes of Fe K-edge and L-edge XAS and 1s2p RIXS, with parameters consistent with ground state DFT simulations of $[Fe(IV)O(H_3buea)]^-$, showing highly covalent σ and π Fe(IV)-oxo bonds.

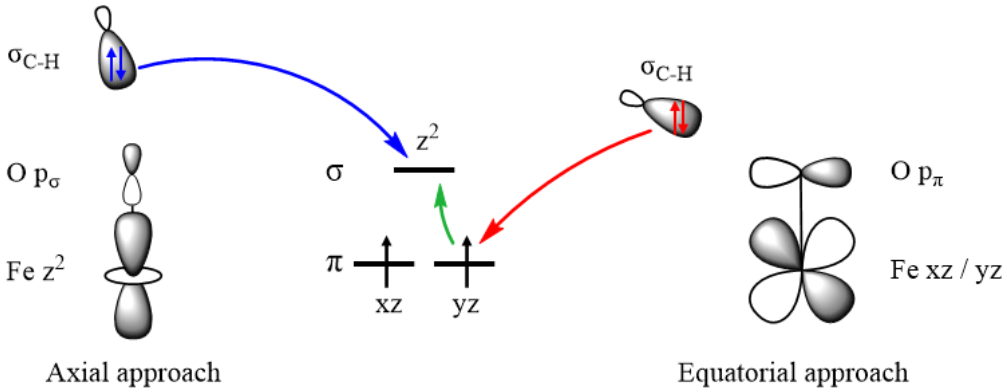

Figure 13: Axial substrate approach (left, blue) through the α 3d(z^2) unoccupied orbital compared with the equatorial approach (right, red) involving the excitation of an α 3d(xz,yz) electron to the 3d(z^2) (green arrow). A higher π-orbital coefficient in the dπ frontier molecular orbitals enables better orbital overlap with the $\sigma_{C\text{-}H}$ orbital of the substrate reacting perpendicular to the Fe=O bond. Adapted from reference 15. Copyright 2020 American Chemical Society.

O K-edge XAS provides complementary insight by specifically probing the O 2p character in the metal valence orbitals. In contrast to the Fe K-edge XAS spectrum where the negligible π-mixing of the O 2p with Fe 4p orbitals results in insignificant transition intensity of the e_π set, the O K-edge directly quantifies the large O 2p π-mixing in the 3d(xz,yz) orbitals. The assignment of the O K-edge XAS spectra in section 2.3 indicates that the 3d(xz,yz) orbitals have approximately twice the O 2pπ character relative to the 3d(z^2) σ-orbital. The 3d(z^2) and 3d(xz,yz) orbitals are the frontier molecular orbitals involved in the reactivity of Fe(IV)=O species that enable axial vs. equatorial attack, respectively, in H atom abstraction and electrophilic aromatic substitution reactions.[14,17,40] In order to allow maximal overlap between the occupied substrate donor $\sigma_{C\text{-}H}$ and the low-lying unoccupied Fe(IV)=O accep-

tor 3d orbitals, the electrophilicity of the Fe(IV)=O species is enhanced by a high orbital coefficient on the O atom, here either in the z^2 for an approach along the Fe=O bond or in the e_π for an approach perpendicular to the Fe=O bond in the reaction. Figure 12A experimentally demonstrates that the e_π orbitals have significant O character (intense peak at 527 eV) consistent with DFT ground state calculations which allow for good overlap of the 3d(xz,yz) orbitals with the substrate $\sigma_{C\text{-}H}$ orbital orientated perpendicular to the Fe-O bond (Figure 13). This is because the 3d(xz,yz) orbitals are strongly antibonding mostly with the O atom. Alternatively, the 3d(z^2) orbital, while having more total covalency than the 3d(xz,yz) orbitals, i.e. less total 3d character (Figure 4), is σ-antibonding with the O atom, but also with the transaxial N atom and to a lesser extent with the equatorial ligand σ-donor orbitals (with the toroid of z^2) of the $[H_3buea]^{3-}$ tripod, hence a lower O character. A recent study[15] showed computationally that on the S_{Fe}=5/2 potential energy surface, the σ-pathway using the 3d(z^2) and the π-pathway, requiring excitation of an electron from the 3d(xz,yz) into the 3d(z^2) orbital (green arrow in Figure 13), had similar reaction barriers despite the additional cost of the dπ to dσ electron promotion.[15] A strongly polarized valence orbital, i.e. a highly covalent Fe-O π-bond, enables this reactivity. The O K-edge XAS data in Figure 12A and its analysis presented above provide the experimental evidence that S=2 Fe(IV)=O sites have large O character in their 3d(xz,yz) π-orbitals allowing the activation of the π-pathway perpendicular to the Fe-O axis, shown to be crucial for the selectivity of Fe(IV)=O intermediates in mononuclear non-heme iron enzymes.[14,17,40]

While TDDFT calculations have the limitations discussed above for the assignment of the pre-edge of the $[Fe(IV)O(H_3buea)]^-$ complex, these do reasonably simulate the significant dipole intensity in the e-orbitals. The knowledge gained in this study of $[Fe(IV)O(H_3buea)]^-$ (including the z^2 α/β splitting) can therefore be used in the context of adjusted TDDFT calculations to understand the pre-edges of enzyme and catalyst intermediates. Here, we analyze the previously reported Fe K-edge XAS spectrum of the S=2 Fe(IV)=O intermediate of TauD[11] reproduced in Figure 14A, after background subtraction.

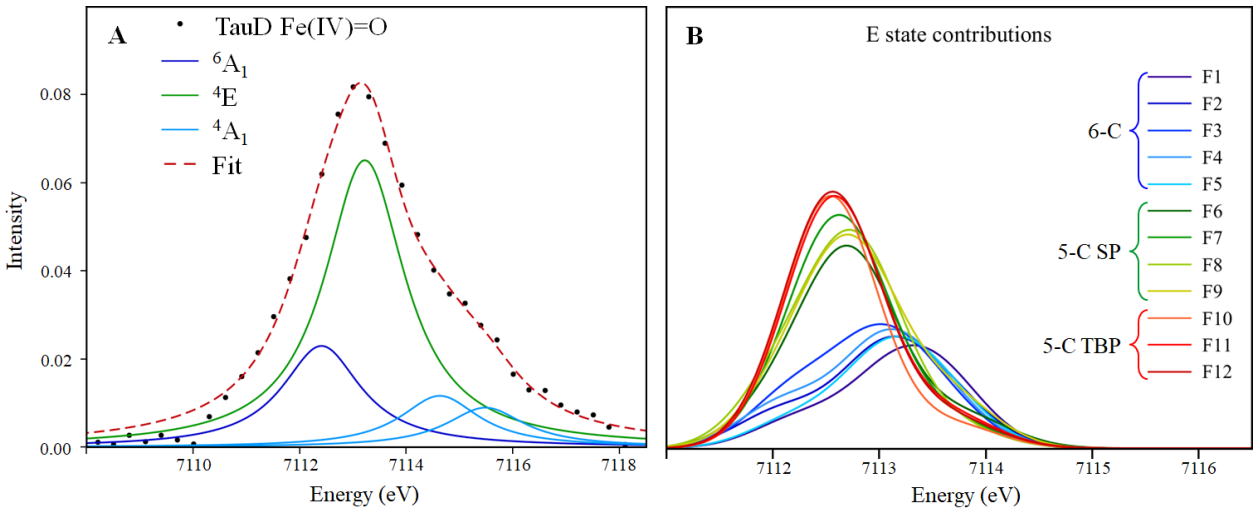

Figure 14: A) Fit of the experimental pre-edge of the Fe(IV)=O intermediate of TauD after background subtraction. Adapted from reference 11. Copyright 2004 American Chemical Society. B) TDDFT-simulated E state contributions to the TDDFT calculations in Figure S14 of the twelve candidate structures for the Fe(IV)=O intermediate of TauD from reference 15 including six-coordinate (F1 to F5, 6-C, blue), five-coordinate square pyramidal (F6 to F9, 5-C SP, green) and five-coordinate trigonal bipyramidal structures (F10 to F12, 5-C TBP, red).

The spectral shape of the pre-edge of the TauD Fe(IV)=O intermediate (Figure 14A) is very similar to the pre-edge of $[Fe(IV)O(H_3buea)]^-$ (Figure 2F), with two peaks at the energy extremes at 7112.4 and 7116.6 eV, and an intense feature in the middle at 7113.2 eV. The pre-edges of the twelve candidate structures built for the previous NRVS study of this intermediate[15] were simulated with the same TDDFT approach as in section 2.1.2 (shown in Figure S14) and the contributions from the E states are shown in Figure 14B. The structures include six-coordinate (blue), five-coordinate square pyramidal with the oxo ligand in the equatorial plane (green) and trigonal bipyramidal (red) structures. The E transitions in the five-coordinate structures (green and red in Figure 14B) are almost twice as intense as the six-coordinate structures (in blue). While the six-coordinate structures have a small amount of $4p_{x,y}$ mixing into the non-z^2 orbitals due to ligand distortions around the iron ion, the spectral shapes of six-coordinate Fe(IV)=O sites (Figure S14 F1 to F5) is dominated by the transitions into the z^2 α and β orbitals. The experimental pre-edge of the Fe(IV)=O intermediate of TauD in Figure 14A with intense transitions into the e_σ orbitals is

only consistent with a five-coordinate structure for this intermediate, in agreement with the analysis from NRVS.[15] It is however not possible to distinguish between trigonal bipyramidal or square pyramidal (with the oxo ligand in the equatorial plane) structures from Fe K-edge XAS as both cases result in significant and comparable dipole intensity in the transitions into the e-orbitals. Fe K-edge XAS can therefore distinguish between five-coordinate and six-coordinate Fe(IV)=O intermediates in enzymes and other catalytic systems. This insight into the Fe K-pre-edge was made possible by combining it with the 1s2p RIXS and L-edge XAS data and their analyses for a structurally-defined model complex. This XAS approach is a powerful characterization technique that complements NRVS and variable temperature MCD, each having specific advantages.

4. Conclusion

The combination of 1s2p RIXS, Fe L-edge XAS and O K-edge XAS with Fe K-edge XAS has been used to rigorously describe the electronic structure of five-coordinate S=2 Fe(IV)=O centers. The loss of inversion in the equatorial plane in the trigonal geometry (D_{3h} and C_{3v} symmetry) gives rise to $4p_{x,y}$-mixing into the $3d(xy,x^2\text{-}y^2)$, adding to the $4p_z$ mixing into the $3d(z^2)$ intensity due to the short Fe=O bond. This structural sensitivity makes Fe K-edge XAS an effective method to probe the geometric structure of Fe(IV)=O sites in protein or catalyst intermediates, as demonstrated for the Fe(IV)=O intermediate of TauD where a 5-coordinate geometry obtained from a previous NRVS study[15] is confirmed by Fe K-edge XAS. The combination of X-ray techniques provides new insight into the different frontier molecular orbitals responsible for electrophilic reactivity. In particular, the O K-edge XAS provides the experimental evidence for the high covalency of the Fe-O π-bond allowing for π-pathway reactivity, despite the axial σ-orbital being exchange-stabilized. The π-pathway enables the reactivity of Fe(IV)=O active sites perpendicular to the Fe=O bond that is important in selectivity.[14,17,40] Over the course of this study, TDDFT calculations

were found to have notable limitations over multiplet simulations of the Fe K-pre-edges when significant exchange interactions are present.

This methodology is now being applied in ongoing studies of S=1 Fe(IV)=O intermediates in non-heme and heme catalysts.

Acknowledgement

This work was supported by the National Institutes of Health (Grant R35GM145202-02 to E.I.S., R37GM050781 to A.S.B. and F32GM122194 to L.B.G.). M.L.B. acknowledges the support of the Human Frontier Science Program, the Royal Society of Chemistry (RM1802-4019) and computing resources provided by STFC Scientific Computing Department's SCARF cluster. Use of the Stanford Synchrotron Radiation Lightsource (SSRL), SLAC National Accelerator Laboratory, is supported by the US Department of Energy (DOE), Office of Science, Office of Basic Energy Sciences under Contract DE-AC02-76SF00515. The SSRL Structural Molecular Biology Program is supported by the DOE Office of Biological and Environmental Research, and by the National Institutes of Health, National Institute of General Medical Sciences (Grant P30GM133894 to K.O.H and B.H). The contents of this publication are solely the responsibility of the authors and do not necessarily represent the official views of NIGMS or NIH. We acknowledge the European Synchrotron Radiation Facility for the provision of synchrotron radiation facilities under proposal number CH4587 and we would like to thank the staff at ID26 for their assistance during the beamtime. Some of the computing for this project was performed on the Sherlock cluster. We would like to thank Stanford University and the Stanford Research Computing Center for providing computational resources and support that contributed to these research results.

Supporting Information Available

Supporting Information. Experimental methods, DFT and multiplet simulation methods and parameters with calculated molecular orbitals and natural transition orbitals, comments on the Slater reduction scaling, additional Fe L-edge and O K-edge XAS data, parameter-dependence on the multiplet simulations of the Fe L-edge XAS, multiplet simulations of the transition dipole tensor components with DOC and state contribution to the CIE cuts of the 1s2p RIXS plane, TDDFT simulations of TauD candidate structures.

References

(1) Vaillancourt, F. H.; Yin, J.; Walsh, C. T. SyrB2 in syringomycin E biosynthesis is a non-heme Fe^{II} α-ketoglutarate- and O_2-dependent halogenase. *Proceedings of the National Academy of Sciences* **2005**, *102*, 10111–10116.

(2) Baldwin, J. E.; Abraham, E. The biosynthesis of penicillins and cephalosporins. *Natural Product Reports* **1988**, *5*, 129.

(3) Vaillancourt, F. H.; Haro, M.-A.; Drouin, N. M.; Karim, Z.; Maaroufi, H.; Eltis, L. D. Characterization of Extradiol Dioxygenases from a Polychlorinated Biphenyl-Degrading Strain That Possess Higher Specificities for Chlorinated Metabolites. *Journal of Bacteriology* **2003**, *185*, 1253–1260.

(4) Mishina, Y.; He, C. Oxidative dealkylation DNA repair mediated by the mononuclear non-heme iron AlkB proteins. *Journal of Inorganic Biochemistry* **2006**, *100*, 670–678.

(5) Solomon, E. I.; DeWeese, D. E.; Babicz, J. T. Mechanisms of O_2 Activation by Mononuclear Non-Heme Iron Enzymes. *Biochemistry* **2021**, *60*, 3497–3506.

(6) Guo, Y.; Chang, W.-C.; Li, J.; Davidson, M. Non-Heme Mono-Iron Enzymes: Co-

Substrate-Dependent Dioxygen Activation, In *Comprehensive Coordination Chemistry III*; Constable, E. C., Parkin, G., Que Jr, L., Eds.; Elsevier: Oxford, 2021; pp 269–300.

(7) Price, J. C.; Barr, E. W.; Tirupati, B.; , B.; Krebs, C. The First Direct Characterization of a High-Valent Iron Intermediate in the Reaction of an α-Ketoglutarate-Dependent Dioxygenase: A High-Spin Fe(IV) Complex in Taurine/α-Ketoglutarate Dioxygenase (TauD) from Escherichia coli. *Biochemistry* **2003**, *42*, 7497–7508.

(8) Fujimori, D. G.; Barr, E. W.; Matthews, M. L.; Koch, G. M.; Yonce, J. R.; Walsh, C. T.; Bollinger, J. M., Jr.,; Krebs, C.; Riggs-Gelasco, P. J. Spectroscopic Evidence for a High-Spin Br-Fe(IV)-Oxo Intermediate in the α-Ketoglutarate-Dependent Halogenase CytC3 from Streptomyces. *Journal of the American Chemical Society* **2007**, *129*, 13408–13409.

(9) Price, J. C.; Barr, E. W.; Hoffart, L. M.; Krebs, C.; Bollinger, J. M., Jr., Kinetic Dissection of the Catalytic Mechanism of Taurine:α-Ketoglutarate Dioxygenase (TauD) from Escherichia coli. *Biochemistry* **2005**, *44*, 8138–8147.

(10) Matthews, M. L.; Neumann, C. S.; Miles, L. A.; Grove, T. L.; Booker, S. J.; Krebs, C.; Walsh, C. T.; Bollinger, J. M., Jr., Substrate positioning controls the partition between halogenation and hydroxylation in the aliphatic halogenase, SyrB2. *Proceedings of the National Academy of Sciences* **2009**, *106*, 17723–17728.

(11) Riggs-Gelasco, P. J.; Price, J. C.; Guyer, R. B.; Brehm, J. H.; Barr, E. W.; Bollinger, J. M., Jr.,; Krebs, C. EXAFS Spectroscopic Evidence for an Fe=O Unit in the Fe(IV) Intermediate Observed during Oxygen Activation by Taurine:α-Ketoglutarate Dioxygenase. *Journal of the American Chemical Society* **2004**, *126*, 8108–8109.

(12) Grzyska, P. K.; Appelman, E. H.; Hausinger, R. P.; Proshlyakov, D. A. Insight into the mechanism of an iron dioxygenase by resolution of steps following the Fe^{IV}=O species. *Proceedings of the National Academy of Sciences* **2010**, *107*, 3982–3987.

(13) Srnec, M.; Wong, S. D.; Matthews, M. L.; Krebs, C.; Bollinger, J. M., Jr.,; Solomon, E. I. Electronic Structure of the Ferryl Intermediate in the α-Ketoglutarate Dependent Non-Heme Iron Halogenase SyrB2: Contributions to H Atom Abstraction Reactivity. *Journal of the American Chemical Society* **2016**, *138*, 5110–5122.

(14) Wong, S. D.; Srnec, M.; Matthews, M. L.; Liu, L. V.; Kwak, Y.; Park, K.; III, C. B. B.; Alp, E. E.; Zhao, J.; Yoda, Y.; Kitao, S.; Seto, M.; Krebs, C.; Bollinger, J. M., Jr.,; Solomon, E. I. Elucidation of the Fe(IV)=O intermediate in the catalytic cycle of the halogenase SyrB2. *Nature* **2013**, *499*, 320–323.

(15) Srnec, M.; Iyer, S. R.; Dassama, L. M. K.; Park, K.; Wong, S. D.; Sutherlin, K. D.; Yoda, Y.; Kobayashi, Y.; Kurokuzu, M.; Saito, M.; Seto, M.; Krebs, C.; Bollinger, J. M., Jr.,; Solomon, E. I. Nuclear Resonance Vibrational Spectroscopic Definition of the Facial Triad Fe^{IV}=O Intermediate in Taurine Dioxygenase: Evaluation of Structural Contributions to Hydrogen Atom Abstraction. *Journal of the American Chemical Society* **2020**, *142*, 18886–18896.

(16) Sinnecker, S.; Svensen, N.; Barr, E. W.; Ye, S.; Bollinger, J. M., Jr.,; Neese, F.; Krebs, C. Spectroscopic and Computational Evaluation of the Structure of the High-Spin Fe(IV)-Oxo Intermediates in Taurine: α-Ketoglutarate Dioxygenase from Escherichia coli and Its His99Ala Ligand Variant. *Journal of the American Chemical Society* **2007**, *129*, 6168–6179.

(17) Srnec, M.; Solomon, E. I. Frontier Molecular Orbital Contributions to Chlorination versus Hydroxylation Selectivity in the Non-Heme Iron Halogenase SyrB2. *Journal of the American Chemical Society* **2017**, *139*, 2396–2407.

(18) Puri, M.; Que, L., Jr., Toward the Synthesis of More Reactive S = 2 Non-Heme Oxoiron(IV) Complexes. *Accounts of Chemical Research* **2015**, *48*, 2443–2452.

(19) Rohde, J.-U.; In, J.-H.; Lim, M. H.; Brennessel, W. W.; Bukowski, M. R.; Stubna, A.;

Münck, E.; Nam, W.; Que, L., Jr., Crystallographic and Spectroscopic Characterization of a Nonheme Fe(IV)=O Complex. *Science* **2003**, *299*, 1037–1039.

(20) Kaizer, J.; Klinker, E. J.; Oh, N. Y.; Rohde, J.-U.; Song, W. J.; Stubna, A.; Kim, J.; Münck, E.; Nam, W.; Que, L., Jr., Nonheme $Fe^{IV}O$ Complexes That Can Oxidize the C-H Bonds of Cyclohexane at Room Temperature. *Journal of the American Chemical Society* **2003**, *126*, 472–473.

(21) England, J.; Martinho, M.; Farquhar, E. R.; Frisch, J. R.; Bominaar, E. L.; Münck, E.; Que, L., Jr., A Synthetic High-Spin Oxoiron(IV) Complex: Generation, Spectroscopic Characterization, and Reactivity. *Angewandte Chemie International Edition* **2009**, *48*, 3622–3626.

(22) Lacy, D. C.; Gupta, R.; Stone, K. L.; Greaves, J.; Ziller, J. W.; Hendrich, M. P.; Borovik, A. S. Formation, Structure, and EPR Detection of a High Spin Fe^{IV}—Oxo Species Derived from Either an Fe^{III}—Oxo or Fe^{III}—OH Complex. *Journal of the American Chemical Society* **2010**, *132*, 12188–12190.

(23) Rohde, J.-U.; Torelli, S.; Shan, X.; Lim, M. H.; Klinker, E. J.; Kaizer, J.; Chen, K.; Nam, W.; Que, L., Jr., Structural Insights into Nonheme Alkylperoxoiron(III) and Oxoiron(IV) Intermediates by X-ray Absorption Spectroscopy. *Journal of the American Chemical Society* **2004**, *126*, 16750–16761.

(24) de Oliveira, F. T.; Chanda, A.; Banerjee, D.; Shan, X.; Mondal, S.; Que, L., Jr.,; Bominaar, E. L.; Münck, E.; Collins, T. J. Chemical and Spectroscopic Evidence for an Fe^{V}-Oxo Complex. *Science* **2007**, *315*, 835–838.

(25) Jackson, T. A.; Rohde, J.-U.; Seo, M. S.; Sastri, C. V.; DeHont, R.; Stubna, A.; Ohta, T.; Kitagawa, T.; Münck, E.; Nam, W.; Que, L., Jr., Axial Ligand Effects on the Geometric and Electronic Structures of Nonheme Oxoiron(IV) Complexes. *Journal of the American Chemical Society* **2008**, *130*, 12394–12407.

(26) Chandrasekaran, P.; Stieber, S. C. E.; Collins, T. J.; Que, L., Jr.,; Neese, F.; DeBeer, S. Prediction of high-valent iron K-edge absorption spectra by time-dependent Density Functional Theory. *Dalton Transactions* **2011**, *40*, 11070.

(27) Ehudin, M. A.; Gee, L. B.; Sabuncu, S.; Braun, A.; Moënne-Loccoz, P.; Hedman, B.; Hodgson, K. O.; Solomon, E. I.; Karlin, K. D. Tuning the Geometric and Electronic Structure of Synthetic High-Valent Heme Iron(IV)-Oxo Models in the Presence of a Lewis Acid and Various Axial Ligands. *Journal of the American Chemical Society* **2019**, *141*, 5942–5960.

(28) Westre, T. E.; Kennepohl, P.; DeWitt, J. G.; Hedman, B.; Hodgson, K. O.; Solomon, E. I. A Multiplet Analysis of Fe K-Edge 1s $\rightarrow$ 3d Pre-Edge Features of Iron Complexes. *Journal of the American Chemical Society* **1997**, *119*, 6297–6314.

(29) Lundberg, M.; Kroll, T.; DeBeer, S.; Bergmann, U.; Wilson, S. A.; Glatzel, P.; Nordlund, D.; Hedman, B.; Hodgson, K. O.; Solomon, E. I. Metal–Ligand Covalency of Iron Complexes from High-Resolution Resonant Inelastic X-ray Scattering. *Journal of the American Chemical Society* **2013**, *135*, 17121–17134.

(30) Kroll, T.; Hadt, R. G.; Wilson, S. A.; Lundberg, M.; Yan, J. J.; Weng, T.-C.; Sokaras, D.; Alonso-Mori, R.; Casa, D.; Upton, M. H.; Hedman, B.; Hodgson, K. O.; Solomon, E. I. Resonant Inelastic X-ray Scattering on Ferrous and Ferric Bis-imidazole Porphyrin and Cytochrome c: Nature and Role of the Axial Methionine–Fe Bond. *Journal of the American Chemical Society* **2014**, *136*, 18087–18099.

(31) Yan, J. J.; Kroll, T.; Baker, M. L.; Wilson, S. A.; Decréau, R.; Lundberg, M.; Sokaras, D.; Glatzel, P.; Hedman, B.; Hodgson, K. O.; Solomon, E. I. Resonant inelastic X-ray scattering determination of the electronic structure of oxyhemoglobin and its model complex. *Proceedings of the National Academy of Sciences* **2019**, *116*, 2854–2859.

(32) Kroll, T.; Baker, M. L.; Wilson, S. A.; Lundberg, M.; Juhin, A.; Arrio, M.-A.; Yan, J. J.; Gee, L. B.; Braun, A.; Weng, T.-C.; Sokaras, D.; Hedman, B.; Hodgson, K. O.; Solomon, E. I. Effect of 3d/4p Mixing on 1s2p Resonant Inelastic X-ray Scattering: Electronic Structure of Oxo-Bridged Iron Dimers. *Journal of the American Chemical Society* **2021**, *143*, 4569–4584.

(33) MacBeth, C. E.; Golombek, A. P.; Young, V. G.; Yang, C.; Kuczera, K.; Hendrich, M. P.; Borovik, A. S. O_2 Activation by Nonheme Iron Complexes: A Monomeric Fe(III)-Oxo Complex Derived From O_2. *Science* **2000**, *289*, 938–941.

(34) MacBeth, C. E.; Gupta, R.; Mitchell-Koch, K. R.; Young, V. G.; Lushington, G. H.; Thompson, W. H.; Hendrich, M. P.; Borovik, A. S. Utilization of Hydrogen Bonds To Stabilize M-O(H) Units: Synthesis and Properties of Monomeric Iron and Manganese Complexes with Terminal Oxo and Hydroxo Ligands. *Journal of the American Chemical Society* **2004**, *126*, 2556–2567.

(35) Wasinger, E. C.; de Groot, F. M. F.; Hedman, B.; Hodgson, K. O.; Solomon, E. I. L-edge X-ray Absorption Spectroscopy of Non-Heme Iron Sites: Experimental Determination of Differential Orbital Covalency. *Journal of the American Chemical Society* **2003**, *125*, 12894–12906.

(36) Hocking, R. K.; Wasinger, E. C.; de Groot, F. M. F.; Hodgson, K. O.; Hedman, B.; Solomon, E. I. Fe L-Edge XAS Studies of $K_4[Fe(CN)_6]$ and $K_3[Fe(CN)_6]$: A Direct Probe of Back-Bonding. *Journal of the American Chemical Society* **2006**, *128*, 10442–10451.

(37) Hocking, R. K.; Wasinger, E. C.; Yan, Y.-L.; deGroot, F. M. F.; Walker, F. A.; Hodgson, K. O.; Hedman, B.; Solomon, E. I. Fe L-Edge X-ray Absorption Spectroscopy of Low-Spin Heme Relative to Non-heme Fe Complexes: Delocalization of Fe d-Electrons into the Porphyrin Ligand. *Journal of the American Chemical Society* **2007**, *129*, 113–125.

(38) Frati, F.; Hunault, M. O. J. Y.; de Groot, F. M. F. Oxygen K-edge X-ray Absorption Spectra. *Chemical Reviews* **2020**, *120*, 4056–4110.

(39) Shadle, S. E.; Hedman, B.; Hodgson, K. O.; Solomon, E. I. Ligand K-edge x-ray absorption spectroscopic studies: metal-ligand covalency in a series of transition metal tetrachlorides. *Journal of the American Chemical Society* **1995**, *117*, 2259–2272.

(40) Neidig, M. L.; Decker, A.; Choroba, O. W.; Huang, F.; Kavana, M.; Moran, G. R.; Spencer, J. B.; Solomon, E. I. Spectroscopic and electronic structure studies of aromatic electrophilic attack and hydrogen-atom abstraction by non-heme iron enzymes. *Proceedings of the National Academy of Sciences* **2006**, *103*, 12966–12973.

(41) Bair, R. A.; Goddard, W. A. Ab initio studies of the x-ray absorption edge in copper complexes. I. Atomic Cu^{2+} and Cu(II)Cl_2. *Physical Review B* **1980**, *22*, 2767–2776.

(42) George, S. D.; Brant, P.; Solomon, E. I. Metal and Ligand K-Edge XAS of Organotitanium Complexes: Metal 4p and 3d Contributions to Pre-edge Intensity and Their Contributions to Bonding. *Journal of the American Chemical Society* **2004**, *127*, 667–674.

(43) George, S. D.; Petrenko, T.; Neese, F. Prediction of Iron K-Edge Absorption Spectra Using Time-Dependent Density Functional Theory. *The Journal of Physical Chemistry A* **2008**, *112*, 12936–12943.

(44) Martin, R. L. Natural transition orbitals. *The Journal of Chemical Physics* **2003**, *118*, 4775–4777.

(45) Haverkort, M. W. Quanty for core level spectroscopy - excitons, resonances and band excitations in time and frequency domain. *Journal of Physics: Conference Series* **2016**, *712*, 012001.

(46) Retegan, M. mretegan/crispy v0.7.3. **2019**. https://doi.org/10.5281/zenodo.3258065.

(47) Snyder, B. E. R. et al. Mechanism of selective benzene hydroxylation catalyzed by iron-containing zeolites. *Proceedings of the National Academy of Sciences* **2018**, *115*, 12124–12129.

(48) Ghiasi, M.; Hariki, A.; Winder, M.; Kuneš, J.; Regoutz, A.; Lee, T.-L.; Hu, Y.; Rueff, J.-P.; de Groot, F. M. F. Charge-transfer effect in hard x-ray 1s and 2p photoemission spectra: LDA+DMFT and cluster-model analysis. *Physical Review B* **2019**, *100*, 075146.

(49) Gupta, R.; Lacy, D. C.; Bominaar, E. L.; Borovik, A. S.; Hendrich, M. P. Electron Paramagnetic Resonance and Mössbauer Spectroscopy and Density Functional Theory Analysis of a High-Spin Fe^{IV}–Oxo Complex. *Journal of the American Chemical Society* **2012**, *134*, 9775–9784.

(50) Tenderholt, A.; Hedman, B.; Hodgson, K. O. PySpline: A Modern, Cross-Platform Program for the Processing of Raw Averaged XAS Edge and EXAFS Data. *AIP Conference Proceedings* **2007**, 105–107.

(51) Neese, F. The ORCA program system. *WIREs Computational Molecular Science* **2012**, *2*, 73–78.

(52) Becke, A. D. Density-functional thermochemistry. III. The role of exact exchange. *The Journal of Chemical Physics* **1993**, *98*, 5648–5652.

(53) Stephens, P. J.; Devlin, F. J.; Chabalowski, C. F.; Frisch, M. J. Ab Initio Calculation of Vibrational Absorption and Circular Dichroism Spectra Using Density Functional Force Fields. *The Journal of Physical Chemistry* **1994**, *98*, 11623–11627.

(54) Becke, A. D. Density-functional exchange-energy approximation with correct asymptotic behavior. *Phys. Rev. A* **1988**, *38*, 3098–3100.

(55) Weigend, F.; Ahlrichs, R. Balanced basis sets of split valence, triple zeta valence and quadruple zeta valence quality for H to Rn: Design and assessment of accuracy. *Physical Chemistry Chemical Physics* **2005**, *7*, 3297.

(56) Weigend, F. Accurate Coulomb-fitting basis sets for H to Rn. *Physical Chemistry Chemical Physics* **2006**, *8*, 1057.

(57) Neese, F. Prediction and interpretation of the ^{57}Fe isomer shift in Mössbauer spectra by density functional theory. *Inorganica Chimica Acta* **2002**, *337*, 181–192.

(58) Tenderholt, A. L. QMForge: Tools for Converting the Output from QM Calculations into Something More Useful, Version 2.4, https://qmforge.net. **2015**,

(59) Rees, J. A.; Martin-Diaconescu, V.; Kovacs, J. A.; DeBeer, S. X-ray Absorption and Emission Study of Dioxygen Activation by a Small-Molecule Manganese Complex. *Inorganic Chemistry* **2015**, *54*, 6410–6422.

(60) König, E.; Kremer, S. *Ligand Field*; Springer US, 1977.

(61) Cowan, R. D. *The Theory of Atomic Structure and Spectra*; University of California Press: Berkeley, 1981.

(62) Lever, A. B. P. *Inorganic electronic spectroscopy*; 1st edition; Elsevier Science Publishers B. V.: Amsterdam, 1968; pp 207–217.

(63) Stout, J. W. Absorption Spectrum of Manganous Fluoride. *The Journal of Chemical Physics* **1959**, *31*, 709–719.

(64) Dingle, R. The Polarized Single Crystal Spectrum of Ammonium Pentafluoromanganate (III). *Inorganic Chemistry* **1965**, *4*, 1287–1290.

(65) Allen, G.; El-Sharkarwy, G.; Warren, K. D. Reinvestigation of the electronic spectrum of potassium hexafluoromanganate(IV). *Inorganic and Nuclear Chemistry Letters* **1969**, *5*, 725–728.

(66) Hocking, R. K.; George, S. D.; Raymond, K. N.; Hodgson, K. O.; Hedman, B.; Solomon, E. I. Fe L-Edge X-ray Absorption Spectroscopy Determination of Differential Orbital Covalency of Siderophore Model Compounds: Electronic Structure Contributions to High Stability Constants. *Journal of the American Chemical Society* **2010**, *132*, 4006–4015.

Supporting information

Experimental and computational methods

Sample preparation. The three complexes K[Fe(IV)O(H_3buea)], K_2[Fe(III)O(H_3buea)] and K[Fe(III)(OH)(H_3buea)] were synthesized following previously published procedures.[22,33,34]

Experimental methods. X-ray experiments have been performed at the Stanford Synchrotron Radiation Lightsource (SSRL) at beamlines 10-1 (Fe L-edge and O K-edge XAS), 9-3 (Fe K-edge) and 6-2 (1s2p RIXS), as well as the European Synchrotron Radiation Facility (ESRF) beamline ID26 (1s2p RIXS). The energy of the Fe K-edge XAS measurements is calibrated using an Fe foil standard, assigning the first inflection point to 7111.2 eV. The incident energy of the 1s2p RIXS and Fe K-edge XAS is calibrated using the first inflection point at 7111.2 eV of an internal Fe foil and the energy transfer with the t_{2g} peak of potassium ferricyanide at the Kα_1. The energy of the L-edge measurements are calibrated using two points of the Fe_2O_3 spectrum as a reference, the maximum intensity of the Fe_2O_3 L_3-edge to 708.5 eV and the maximum of the lower-intensity L_2 feature to 720.1 eV.

K-edge XAS spectra were background subtracted, splined, and normalized using the PYSPLINE software.[50] The Fe K-pre-edge intensity was calculated using a trapezoid integration method which gives similar results to the Simpson's integration method.[26] For Fe L-edge XAS spectra, a background function was first subtracted from each spectra, to which two arctangent functions were used to model the L_3- and L_2-edge jumps.[35] The 1s2p RIXS plane intensity was normalized using long scans measured beyond the edge jump using the software Igor Pro.[29]

Density Functional Theory calculations. All calculations were carried out using the quantum chemistry program ORCA[51] (version 4.0.1.2). Single point calculations and optimizations were performed with the functionals B3LYP,[52,53] BP86[54] and BP86 with 10% Hartree-Fock exchange (commonly used for the optimization of open-shell molecules), and the standard polarized triple-ζ basis set def2-TZVPP[55] and auxiliary basis set def2/J[56] and

def2-TZVPP/C and CP(PPP) on the iron ion.[57] The comparison of the geometry of the optimized structures with the different functionals and non-optimized crystal structures of the three compounds only show minimal changes (Table S2). Since the solid samples were experimentally measured, the electronic structures of the three compounds is presented in the main text in their crystal structure geometries. Löwdin population analyses were performed using the QMForge Suite.[58] For Time-Dependent Density Functional Theory calculations, the functionals B3LYP, BP86 and BP86 with 10% HF were used with the same basis set as for optimizations and a very dense integration grid (grid6) and tight convergence criteria were enforced. TDDFT simulations of metal K-edge pre-edges with the B3LYP functional were previously considered to give a good agreement with experimental data[32,59] and are the simulations presented in the main text. The use of BP86 and BP86 with 10% Hartree-Fock exchange produced similar results with the differences highlighted in Table S3. Calculated K-pre-edge spectra were visualized using the ORCA_MAPSPC module with a Gaussian broadening of 1.0 eV. The intensity was scaled and the energy was shifted to be comparable with the experimental data.

Multiplet simulations. Calculations were carried out using Quanty,[45] Version 0.6. The trigonal ligand-field matrix of the Fe 3d orbitals in C_{3v} symmetry is parameterised by two variables $D\tau$ and $D\sigma$, where the matrix elements are given as follows:[60]

$$\begin{aligned}
\langle e_\pi \mid V \mid e_\pi \rangle &= -4Dq + D\sigma + \frac{2}{3}D\tau \\
\langle e_\sigma \mid V \mid e_\sigma \rangle &= 6Dq + \frac{7}{3}D\tau \\
\langle a_1 \mid V \mid a_1 \rangle &= -4Dq - 2D\sigma - 6D\tau \\
\langle e_\pi \mid V \mid e_\sigma \rangle &= -\frac{\sqrt{(2)}}{3}(3D\sigma - 5D\tau).
\end{aligned}$$

The off-diagonal term mixes 1/3 e_π into e_σ and 1/3 e_σ into e_π. Atomic Slater integrals and spin-orbit coupling constants were calculated from Hartree-Fock theory using Cowan's atomic multiplet structure package.[61] The ligand field diagram plotted as a function of

Slater integral (F_2 and F_4) scaling was calculated using the *Eigensystem* function including all 252 states of the $3d^5$ configuration and excluded $3d$ spin-orbit coupling. Final states that are accessible in the K-pre-edge were selected by analysing S^2 and orbital electron occupation expectation values. Decomposition of the Fe L-edge XAS spectrum into ligand-field components were obtained by the inclusion of the $\{'Tensor', true\}$ keywords in the *CreateSpectra* function. Quanty input files for the simulation of $L_{2,3}$-edge XAS and 1s2p RIXS spectra were edited from input files generated using Crispy.[46] 1s2p RIXS intensities were calculated as quadrupole before scaling to account for the enhancement of intensity due to the presence of dipole transition character. All were scaled relative to E_σ, giving the total intensity as E_σ + 0.6 x A_1 + 0.06 x E_π. Differential orbital covalency was included using the previously reported methods.[35–37] The parameters for multiplet and VBCI fits are given in Table S1. The 2p spin-orbit coupling constant ζ_{2p} is 5% larger than the atomic value (8.1991 eV) to match the experimental energy splitting between the L_3 and L_2 edges. For the 1s2p RIXS plane simulations, the broadening in the incident energy direction is 1.25 eV and in the emission energy is 0.8 eV. For Fe L-edge XAS simulations, a Gaussian broadening with FWHM 0.47 eV was applied, along with a Lorentzian broadening with FWHM 0.4 eV in the L_3-edge and 1.4 eV in the L_2-edge.

Comments on the Slater reduction scaling

Previous analysis of Fe(II) compounds gave Slater integral scaling factors of 70-80% and Fe(III) compounds of 60-70%.[30,31] Since Fe(IV) compounds are more covalent, an increase of nephelauxetic reduction of the electronic repulsion is expected (i.e. a further decrease in Slater integral scaling). This decrease upon oxidation is observed in the nephelauxetic series.[62] As an example, the Racah parameter and nephelauxetic parameter β of Mn(II), Mn(III) and Mn(IV) with fluoride ligands can be estimated from the sharp d-d spin-flip transitions in the electronic absorption spectra. The $^6A_{1g} \rightarrow {}^4A_{1g}$ transition at 23190 cm^{-1} for $Mn(II)F_2$[63] gives β=0.91, the $^5E_g \rightarrow {}^3E_g/{}^3T_{2g}/{}^3A_{1g}/{}^3A_{2g}$ at 16700 cm^{-1} for $(NH_4)_2Mn(III)F_5$[64]

gives β around 0.77 and the $^4A_{2g} \rightarrow {}^2E_g/{}^2T_{2g}$ at 14000 cm^{-1} for $K_2Mn(IV)F_6$[65] gives β=0.55. Thus there is a more pronounced decrease in going from Mn(III) to Mn(IV) than from Mn(II) to Mn(III). A parallel trend is expected for Fe(II) to Fe(III) to Fe(IV). Using the ratio of nephelauxetic parameter of Mn fluoride compounds, a Slater integral scaling of 75% for ferrous compounds goes down to 63% for Fe(III) compounds and down to 45% for Fe(IV) compounds. In $[Fe(IV)O(H_3buea)]^-$, the presence of a highly covalent oxo-ligand can tune this value even lower to the 35-45% range used in this study (the final atomic multiplet fit uses 37% while including DOC in the multiplet simulations result in a scaling of 42%).

Additionally, multiplet simulations using a Slater integral scaling lower than 24% for a trigonal ligand field with a 0.68 eV gap between the e_π and e_σ orbital sets gives an S=0 ground state (i.e. an $e_\pi{}^4e_\sigma{}^0$ configuration) instead of a S=2 ground state ($e_\pi{}^2e_\sigma{}^2$ configuration) due to the significantly lower electron-electron repulsion, as shown on Figure S1: for a Slater integral scaling below 20%, the simulated Fe K-edge XAS spectra consist of two main contributions split by about 1.6 eV, the splitting of the e_σ and z^2 orbitals, with a 2:1 intensity ratio, indicating an S=0 ground state; above 27%, the multiplet simulations give an S=2 ground state. Significantly mixed wavefunctions are obtained for a Slater integral scaling between 20 and 27%.

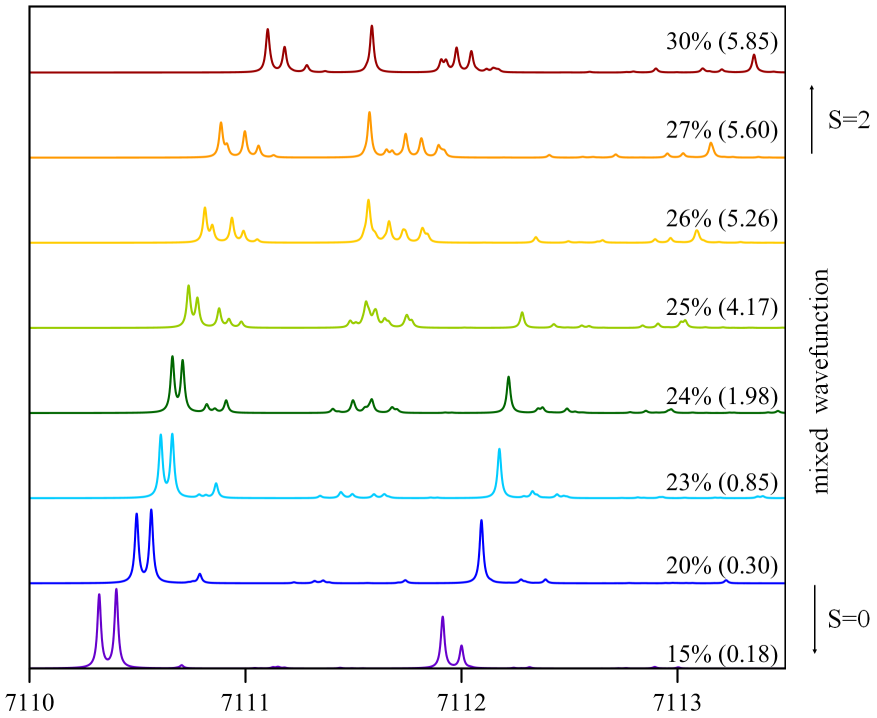

Figure S1: Multiplet Fe K-edge XAS simulations showing the transition between a low-spin and high-spin ground state upon changing the Slater integral scaling (indicated for each simulation), using the atomic multiplet parameters listed in Table S1. The spin expected value $\langle S^2 \rangle$ of the ground state is given between parentheses for each spectrum. A 0.01 eV-Lorentzian broadening was applied to better visualize the states.

Supporting figures and tables

Table S1: Multiplet and charge transfer multiplet parameters in eV for [Fe(IV)O(H_3buea)]$^-$ Fe L-edge XAS and 1s2p RIXS simulations. The parameter κ is a scale factor that reduces the atomic Slater integrals obtained from Hartree Fock Theory to account for the nephelauxetic effect.

	Dq	$D\tau$	$D\sigma$	κ	Δ_i	Δ_f	$V_{e\pi}$	$V_{e\sigma}$	V_{a1}	ζ_{2p}
Atomic multiplet	0.0	-0.12	-0.42	0.37	-	-	-	-	-	8.6091
CT multiplet	0.0	-0.196	-0.333	0.42	2.0	1.0	2.27	3.03	2.49	8.6091

Table S2: Comparison of relevant bond length and angle averages of the crystal structure and optimized geometry for [Fe(III)(OH)(H_3buea)]$^-$, [Fe(III)O(H_3buea)]$^{2-}$ and [Fe(IV)O(H_3buea)]$^-$ with the functionals BP86/B3LYP. The distances are given in angstrom and the angles in degrees.

	[Fe(III)(OH)(H_3buea)]$^-$		[Fe(III)O(H_3buea)]$^{2-}$		[Fe(IV)O(H_3buea)]$^-$	
	crystal	optimized	crystal	optimized	crystal	optimized
Fe-O	1.93	1.96/1.92	1.81	1.80/1.78	1.68	1.69/1.66
Fe-N_{ax}	2.17	2.25/2.26	2.28	2.35/2.35	2.06	2.09/2.10
Fe-N_{eq}	2.02	2.03/2.04	2.06	2.07/2.09	1.98	2.00/2.00
O-Fe-N_{eq}	100	101/100	101	102/102	98	97/98

Table S3: Comparison of the e_π and e_σ orbital population, the intensity ratio of the transitions into the e_π and e_σ orbitals and the splitting of the transitions into the z^2 α and β orbitals in the TDDFT simulation of [Fe(IV)O(H_3buea)]$^-$ with different functionals.

	B3LYP	BP86 10% HF	BP86
e_σ character in e_π orbitals	23%	27%	28%
e_π character in e_σ orbitals	20%	23%	26%
e_π/e_σ intensity ratio	1.32	0.87	0.65
z^2 α/β splitting (in eV)	0.97	1.18	1.27

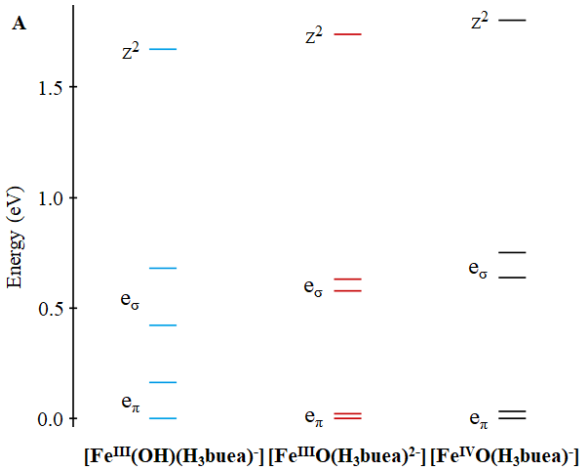

B

MO	$[Fe^{III}(OH)(H_3buea)]^-$	$[Fe^{III}O(H_3buea)]^{2-}$	$[Fe^{IV}O(H_3buea)]^-$
e_π β	85	71	67
e_σ β	69	69	65
z^2 β	68	63	57

Figure S2: A) Energy diagram of the β-manifold for $[Fe(III)(OH)(H_3buea)]^-$, $[Fe(III)O(H_3buea)]^{2-}$ and $[Fe(IV)O(H_3buea)]^-$. The e_π and e_σ of $[Fe(IV)O(H_3buea)]^-$ and $[Fe(III)O(H_3buea)]^{2-}$ are tilted due to the C_{3v} symmetry allowing mixing of the two e-sets. B) Molecular orbital population analysis of the unoccupied 3d orbitals of $[Fe(III)(OH)(H_3buea)]^-$, $[Fe(III)O(H_3buea)]^{2-}$ and $[Fe(IV)O(H_3buea)]^-$. The average of amount of Fe 3d-character in percent is given for each orbital set.

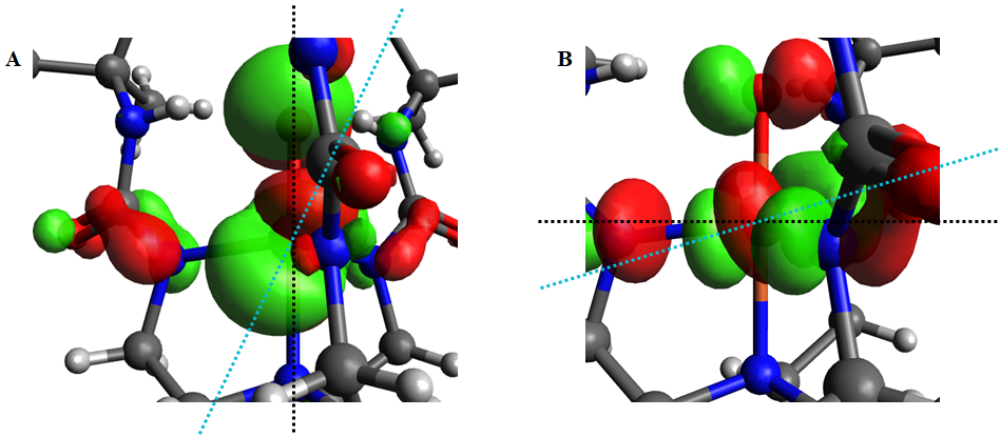

Figure S3: Overlap of the calculated Fe 3d orbitals with the $[H_3buea]^{3-}$ ligand. A) The axis of the e_π is shown in light blue with the Fe-O bond axis in black. The tilt of the orbital allows the overlap with the urea π-orbital on the left. B) The axis of the e_σ is shown in light blue with the equatorial plane of the iron in black. A first factor for this tilt is the π-interaction of the Fe 3d with the π-orbitals of the urea moieties of the ligand (mostly visible on the left of A). A second factor is the iron atom being 0.26 Å above the equatorial plane of the three ligating nitrogen atoms, and therefore the Fe-N bonds not being in this plane (mostly visible on B). This tilt is reflected in the population analysis (Table S3) where 23% of the 3d character in the e_π orbitals has e_σ character and 20% of the 3d character in the e_σ orbitals has e_π character. This tilt angle of the e-orbitals in C_{3v} symmetry is functional-dependent and increases with decreasing Hartree-Fock exchange mixing (Table S3).

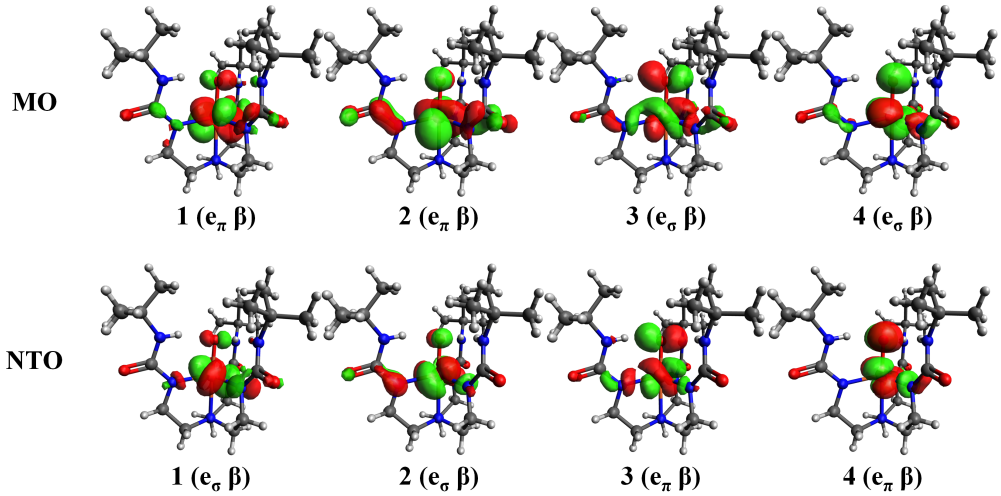

Figure S4: Top: Isosurface plots of the four ground state MOs of the two e-orbitals sets of $[Fe(III)O(H_3buea)]^{2-}$, in increasing orbital energy order. The e-orbitals are tilted, indicating mixing of the two sets of e-orbitals, similar to the MOs for $[Fe(IV)O(H_3buea)]^{-}$ shown in Figure S3. Bottom: Isosurface plots of the four acceptor NTOs corresponding to the transitions into the e-orbitals of $[Fe(III)O(H_3buea)]^{2-}$, in increasing transition energy order. The e_π-like NTOs are the two higher energy NTOs and the e_σ-like NTOs are the two lower energy NTOs, which is a flipped order compared with the ground state MOs. The acceptor NTOs of the e sets are less tilted as the two lower energy e NTOs lose most of their overlap with the axial oxo and become mostly σ-antibonding with the $[H_3buea]^{3-}$ ligand in the equatorial plane, and the two higher energy NTOs become more π-antibonding with the axial oxo in the final state. This electronic relaxation shifts the dipole character into the lowest energy e peak, while experimentally it has more intensity in the higher energy peak.

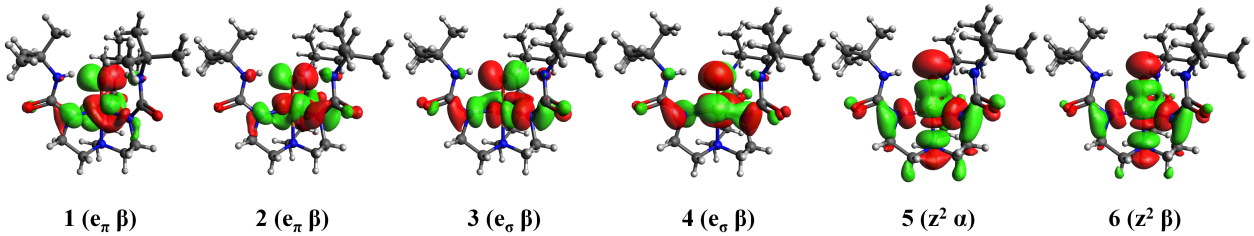

Figure S5: Isosurface plots of the six acceptor NTOs corresponding to the pre-edge transitions of $[Fe(IV)O(H_3buea)]^{-}$, in increasing transition energy order.

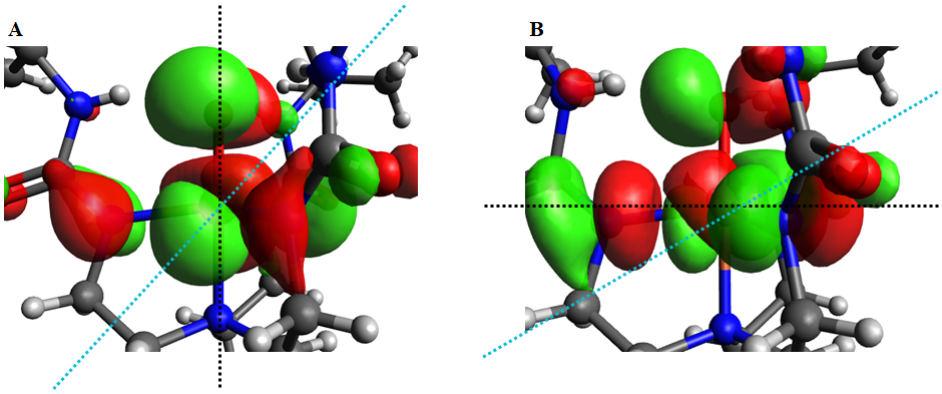

Figure S6: Acceptor NTOs for [Fe(IV)O(H_3buea)]$^-$. A) The axis of the acceptor NTO of the transition at 7112.83 eV (e_π-like) is shown in light blue with the Fe-O bond axis in black. B) The axis of the acceptor NTO of the transition at 7113.63 eV (e_σ-like) is shown in light blue with the equatorial plane in black. The tilt angle and the distribution of dipole intensity in the two sets of transitions is functional-dependent with the e_σ transferring less intensity into the e_π as the Hartree-Fock exchange is increased (Table S3).

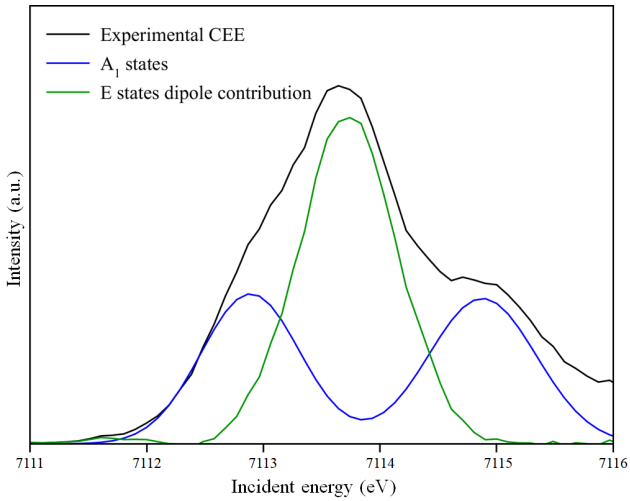

Figure S7: Experimental dipole contribution in the E states (green) obtained by subtracting the $^6A_1$ and $^4A_1$ states (shown in blue, split by 2 eV), obtained by fitting the CEE, from the total experimental CEE of [Fe(IV)O(H_3buea)]$^-$ (black).

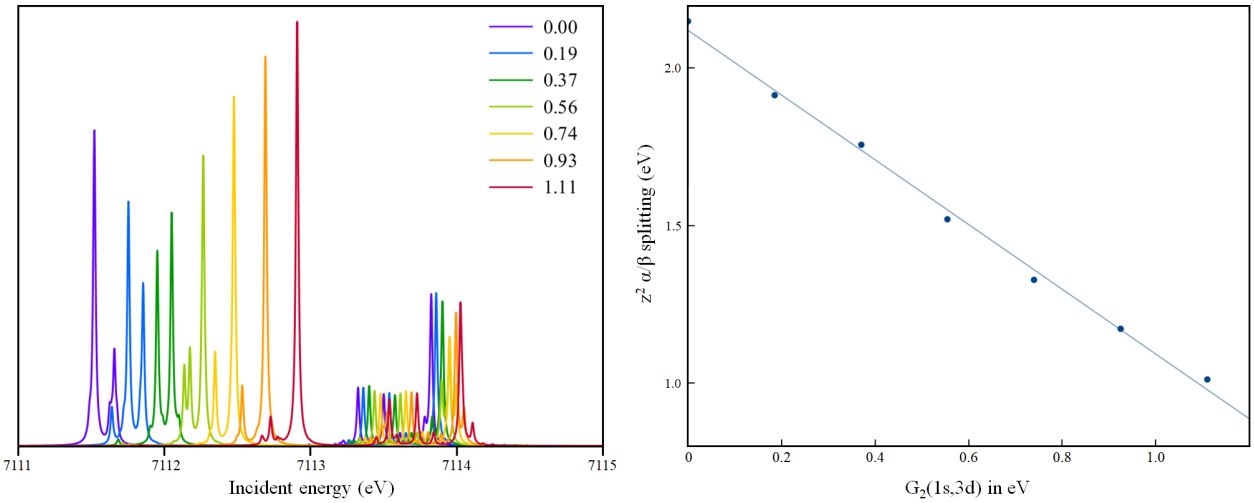

Figure S8: Left: Contribution of A_1 states to a K-pre-edge plotted with a narrow Lorentzian broadening of 0.01 eV for increasing G_2(1s,3d). The splitting of the A_1 states decreases as G_2(1s,3d) increases. The Hartree Fock calculated value is 0.0733 eV. Right: Splitting of the center of mass of the 1s $\rightarrow$ z^2 α and β transitions as a function of the magnitude of G_2(1s,3d).

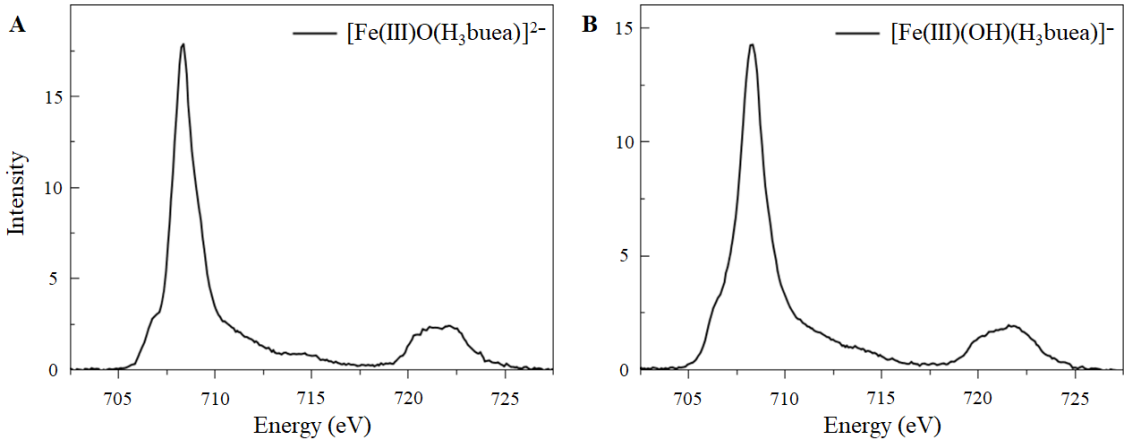

Figure S9: Fe L-edge XAS spectra of A) $[Fe(III)O(H_3buea)]^{2-}$ and B) $[Fe(III)(OH)(H_3buea)]^{-}$.

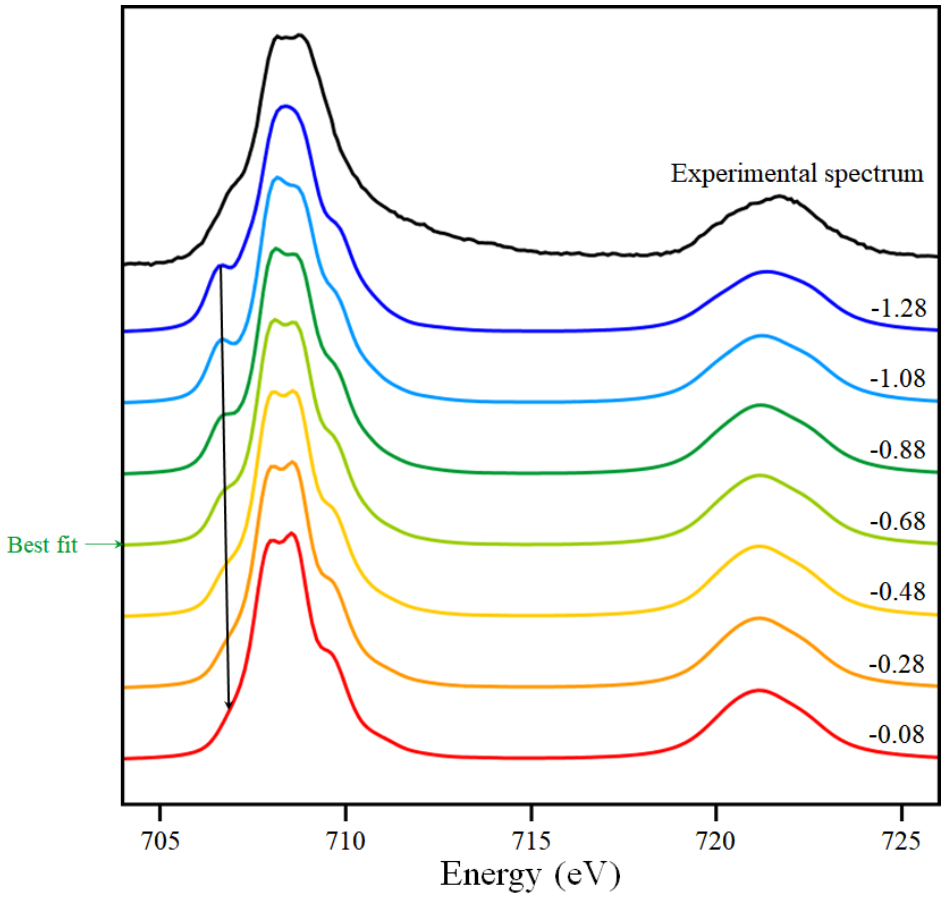

Figure S10: Multiplet simulated spectra of the Fe L-edge XAS spectrum of $[Fe(IV)O(H_3buea)]^-$ upon shifting the energy of the e_π orbitals relative to the e_σ orbitals while keeping the other atomic multiplet parameters at the values listed in Table S1. The experimental spectrum is shown in black and the best fit to the experiment is indicated by an horizontal arrow. The number on the right is the energy difference between the e_π and e_σ orbitals in eV. The black line emphasizes the shift of the low-energy feature.

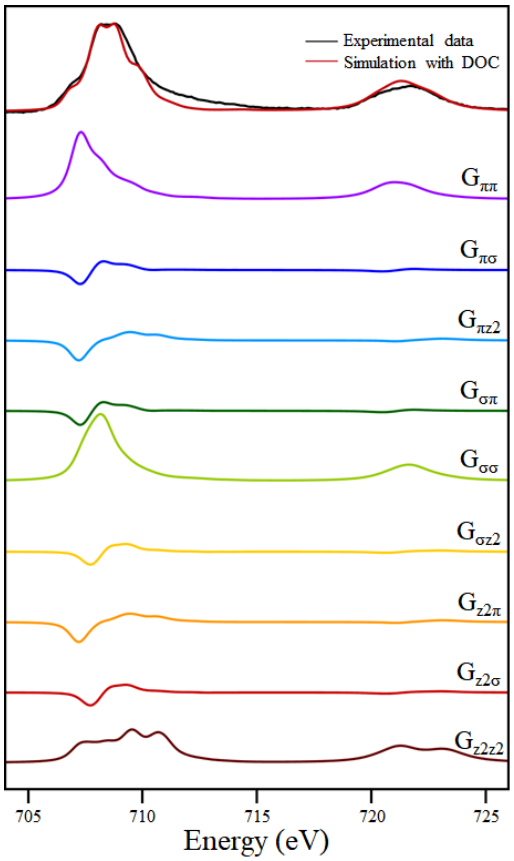

	Multiplet only	With DOC
$G_{\pi\pi}$	1.775	1.774
$G_{\sigma\sigma}$	1.854	1.832
G_{z2z2}	1.590	1.577
$G_{\pi\sigma}$	0.008	0.002
$G_{\pi z2}$	-0.026	-0.036
$G_{\sigma z2}$	-0.006	-0.008

Figure S11: Left: Multiplet simulation of the Fe L-edge XAS spectrum including DOC (top) with the G_{ij} components of the calculated transition dipole operator including DOC, using the CT multiplet parameters listed in Table S1. Right: Comparison of the integrated intensity of the different G_{ij} without and with DOC. Aside from small intensity changes of G_{ij} due to the inclusion of the covalency differences of the 3d orbitals, as calculated by DFT (Figure 4), no significant change is observed in the simulations with and without DOC. DOC is crucial for the proper simulation of low spin compounds,[35–37,66] since the t_{2g} and e_g orbitals which have very different covalency contributions in different parts of the spectrum. The effect of DOC is less pronounced in high spin compounds as the contribution of the t_{2g} and e_g orbitals spreads over most of the L_3-edge. For a trigonal Fe(IV)=O, the e_π and e_σ orbitals contribute to different parts of the L_3-edge but have similar 3d character (see Figure 4), while the z^2 orbital, while more covalent than the e_π and e_σ orbitals, has contributions spread over the entire L_3-edge. As a result, the introduction of DOC only scales down the total intensity of the L_3-edge.

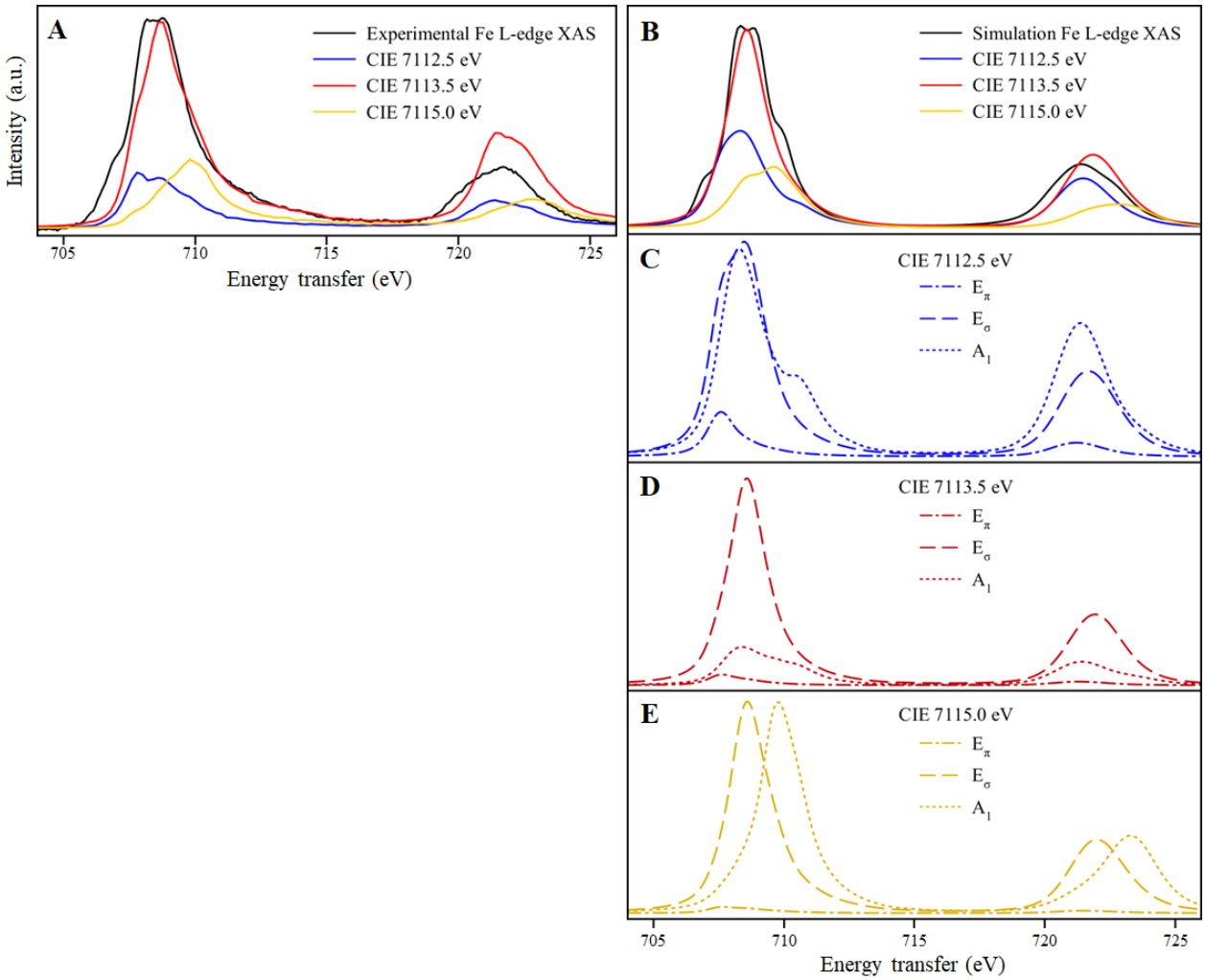

Figure S12: A) Overlap of the experimental Fe L-edge XAS spectrum (black) with the CIE cuts as shown in Figure 11. The 7112.5 eV CIE cut (blue) has its maximum at 707.1 eV that corresponds to the rising side of the L_3-edge with an intense tail to higher energies. The 7113.5 eV CIE cut (red) has its maximum at 708.0 eV that corresponds to the high-energy side of the flat top of the L_3-edge, with a low-energy shoulder and high-energy tail. The 7115.0 eV CIE cut (yellow) has its maximum at 709.1 eV that corresponds to the high-energy side of the L_3-edge and is preceded by a low-energy tail. The significant tails are due to the non-negligible lifetime broadening in the incident energy direction resulting in feature overlap, along with strong multiplet mixing of states involving 2p and 3d unpaired electrons. The splitting of the maxima of the 7112.5 and 7115.0 eV CIE cuts is close to 2 eV and reflects the large amplitude of the splitting of the $^6A_1$ and $^4A_1$ states. B) Simulated CIEs of $[Fe(IV)O(H_3buea)]^-$ using the atomic multiplet parameters from Table S1. C) Specific state contributions to the CIE at 7112.5 eV, mostly A_1 and E_σ contribution, with the E_π states very weak as they have no dipole chaaracter in the Fe K-pre-edge. D) Specific state contributions to the CIE at 7113.5 eV, essentially only the E_σ-contribution. E) Specific state contributions to the CIE at 7115.0 eV, significant A_1 and E_σ contributions even though the CEE simulations show little E_σ contribution at this energy. E_σ-character in these L-edge-like final states comes from significant multiplet mixing between those states, as seen in the $G_{\sigma z^2}$ component of the transitions dipole tensor (Figure 10).

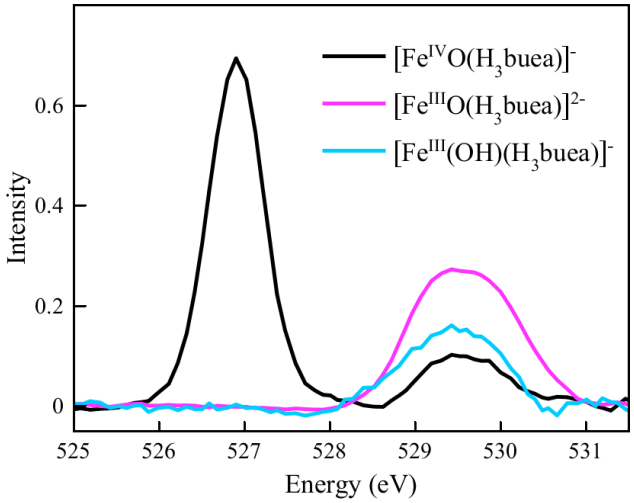

Figure S13: Background-subtracted O K-pre-edge of $[Fe(IV)O(H_3buea)]^-$ (black), $[Fe(III)O(H_3buea)]^{2-}$ (pink) and $[Fe(III)(OH)(H_3buea)]^-$ (blue).

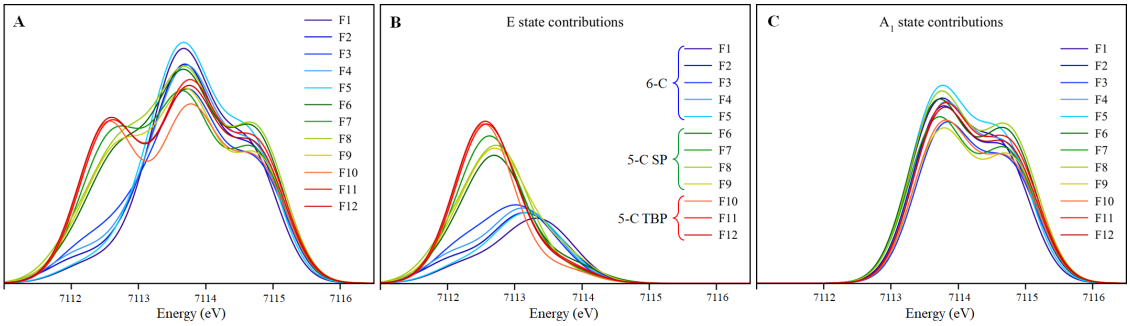

Figure S14: A) TDDFT-simulated spectra of the twelve candidate structures for the TauD Fe(IV)=O intermediate from reference 15 with six-coordinate (F1 to F5, 6-C, blue), five-coordinate square pyramidal (F6 to F9, 5-C SP, green) and five-coordinate trigonal bipyramidal structure (F10 to F12, 5-C TBP, red). B) Corresponding TDDFT-simulated E state contributions structures as shown in Figure 14. C) Corresponding TDDFT-simulated A_1 state contributions. The XYZ cartesian coordinates of each structure can be found in the Supporting Information of reference 15.

TOC Graphic

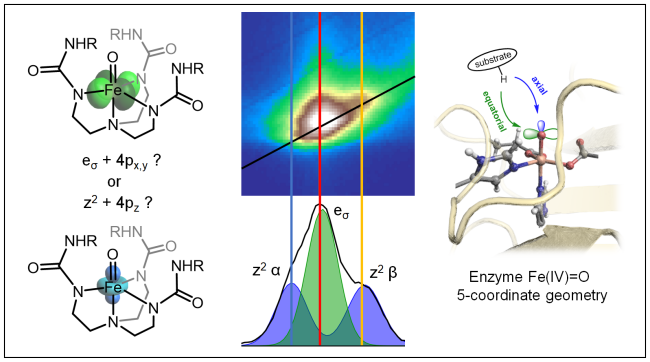
NHR
RHN
O
N
Fe
NHR
$e_\sigma + 4p_{x,y}$?
or
$z^2 + 4p_z$?
e_σ
z^2 α
z^2 β
substrate
H
axial
equatorial
O
Enzyme Fe(IV)=O
5-coordinate geometry